OncoVision: Integrating Mammography and Clinical Data through Attention-Driven Multimodal AI for Enhanced Breast Cancer Diagnosis

Istiak Ahmed^{1,4}, Galib Ahmed^{2,4}, K. Shahriar Sanjid^{1,4}, Md. Tanzim Hossain^{3,4}, Md. Nishan Khan^{1,4}, Md. Misbah Khan^{1,4}, Md Arifur Rahman⁵, Sheikh Anisul Haque⁶, Sharmin Akhtar Rupa⁷, Mohammed Mejbahuddin Mia⁸, Mahmud Hasan Mostofa Kamal ⁹, Md. Mostafa Kamal Sarker¹⁰, M. Monir Uddin^{2,4*}

^{1*}Department Electrical and Computer Engineering , North South University, Dhaka, 1229, Bangladesh.

²Department of Mathematics and Physics , North South University, Dhaka, 1229, Bangladesh.

³Department of Data Science , Friedrich-Alexander University, Erlangen, 91054, Germany.

 ⁴Big-Matrix Lab, North South University, Dhaka, 1229, Bangladesh.
 ⁵Department of Oncology & Radiotherapy, Bangladesh Specialized Hospital, Shyamoli, Dhaka, 1207, Dhaka, Bangladesh.

⁶Department of Transfusion Medicine, Bangladesh Specialized Hospital, Shyamoli, Dhaka, 1207, Dhaka, Bangladesh.

⁷Department of Radiology & Imaging, Popular Medical College, 21 Shyamoli, Dhaka, 1205, Dhaka, Bangladesh.

⁸Department of Transfusion Medicine, Khwaja Yunus Ali Medical College & Hospital, Enayetpur, Sirajganj, 6751, Rajshahi, Bangladesh.

⁹Department of Radiology and Imaging , Bangladesh Medical University, Shahbag, Dhaka, 1000, Bangladesh.

¹⁰Department of Oncology, University of Cambridge, Cambridge Biomedical Campus, Cambridge, CB2 0SP, United Kingdom.

*Corresponding author(s). E-mail(s): monir.uddin@northsouth.edu;
Contributing authors: istiak.ahmed1@northsouth.edu;
galib.ahmed.251@northsouth.edu; kazi.sanjid@northsouth.edu;
tanzim.hossain@fau.de; nishan.khan@northsouth.edu;
misbah.khan@northsouth.edu; drarifur@bshl.com.bd; dr.anisul@bshl.com.bd;
dr.sharminakhtarrupa@yahoo.com; drmejbah2013@gmail.com;
mkamal@bsmmu.edu.bd; mmks3@.cam.ac.uk;

Abstract

OncoVision is a multimodal AI pipeline that combines mammography images and clinical data for better breast cancer diagnosis. Employing an attention-based encoder-decoder backbone, it jointly segments four ROIs – masses, calcifications, axillary findings, and breast tissues – with state-of-the-art accuracy and robustly predicts ten structured clinical features: mass

morphology, calcification type, ACR breast density, and BI-RADS categories. To fuse imaging and clinical insights, we developed two late-fusion strategies. By utilizing complementary multimodal data, late fusion strategies improve diagnostic precision and reduce inter-observer variability. Operationalized as a secure, user-friendly web application, OncoVision produces structured reports with dual-confidence scoring and attention-weighted visualizations for real-time diagnostic support to improve clinician trust and facilitate medical teaching. It can be easily incorporated into the clinic, making screening available in underprivileged areas around the world, such as rural South Asia. Combining accurate segmentation with clinical intuition, OncoVision raises the bar for AI-based mammography, offering a scalable and equitable solution to detect breast cancer at an earlier stage and enhancing treatment through timely interventions.

Keywords: Multimodal Pipeline in Mammography, Breast Cancer Diagnosis, Clinical Feature Prediction, Structured Reporting, Lesion Segmentation

1 Main

Breast cancer is the leading cause of cancer death in women worldwide. Early diagnosis of breast cancer is crucial for improving the survival and decreasing the treatment cost [1-4]. Mammography is the most common method to detect the abnormalities in breast. Tissue, mass, calcification and axilla findings can be observed in mammogram as different ROIs which helps to indicate the risk stratification by a standardize frameworks like Breast Imaging Reporting and Data System (BI-RADS) and American college of Radiology breast (ACR) density classifications [5–7]. Despite being a widely used technique, much variability in the interpretation of mammograms is observed (mainly because of subjective differences between radiologists), and low contrast microcalcifications or high breast density commonly result in false negatives, especially for isodense masses of spiculated outline and complex BI-RADS 4 and 5 [8–11]. These problems are even more severe in resource-poor areas, where expert radiologists and complex imaging devices are not widely available, accentuating the urgency of automated diagnostic methods to aid bedside diagnostics [12–15]. Artificial intelligence (AI) is expected to radically improve mammography by automating detection, segmentation and risk analysis, which would lead to more precise and accessible diagnosis [16-18]. Nevertheless, most of the current AI-based models just accomplish isolated tasks that are detecting a specific abnormality or predicting a single clinical sign and show partial support for diagnosis. [19, 20]. All-encompassing AI pipelines for multiple diagnostic tasks (interpretable whenever possible) are required for clinical deployment, especially in life-threatening scenarios with non-obvious findings such as microcalcifications or borderline BI-RADS categories [21–23]. Deployable AI solutions that easily fit into a hospital workflow and can help not only radiologists, but also medical students, residents, and practicing clinicians in underserved regions are also essential for overcoming disparities in breast cancer care [24–26].

This study introduces OncoVision, the first end-to-end multimodal AI pipeline to annotate four segmentation features—masses, calcifications, axillary findings, and breast tissue—within a single mammogram, while simultaneously predicting ten clinical features: mass presence, mass definition (well-defined, ill-defined, spiculated), mass density (low, isodense, high), mass shape (oval, round, irregular), mass calcification, axillary findings, calcification presence and distribution (discrete, clustered, line/segmental), ACR breast density (fatty/normal, fibroglandular/mixed, heterogeneously dense, highly dense), and BI-RADS categories (1–6). OncoVision employs two late fusion variants to enhance predictive accuracy, addressing challenges in detecting critical features such as isodense masses, spiculated masses, and BI-RADS categories 4 and 5, which are pivotal for risk stratification [27–29]. A reader study validated OncoVision's interpretability (Extended Data Fig. 8), demonstrating that its outputs provide confidence to radiologists by highlighting clinically relevant patterns, particularly in complex cases [30, 31]. OncoVision annotates up to four types of lesions (masses, calcification, axillary findings and breast tissue) to help support a complete diagnosis for patients with suspicion of Breast Cancer. Spiculated or irregular mass may represent malignancy and must be defined accurately [7, 29]. Line/segmental microcalcification to detect ductal carcinoma in situ (DCIS) in an early stage [32, 33]. The axilla determines staging and treatment [34, 35]. Finally, breast tissue is used to contextualize the ROIs, adjust for density and remove non-correlated structures [36, 37]. All characteristics are consistent with clinical guidelines, and if any of them is removed the analysis becomes incomplete [5, 6, 34, 37]. This supports use of structured diagnostic reports, which reflects radiologist behavior [27, 30]. The dataset, obtained from Bangladesh Specialized Hospital Limited (urban, Dhaka) and Khwaja Yunus Ali Medical College & Hospital (rural, Rajshahi), consists of 1725 high-quality mammograms capturing both craniocaudal and mediolateral oblique views from total 500 patients. This diversity in both geography and socioeconomic status allows for generalizability to a wide range of clinical settings, particularly those with fewer resources where diagnostic inequalities are common [15, 20]. This geographic and socioeconomic diversity ensures generalizability across varied clinical settings, particularly in resource-limited environments where diagnostic disparities are prevalent [13, 14]. Stringent quality control procedures led to the removal of images with artifacts, poor contrast and improper positioning by the expert radiologists ensuring diagnostic relevance [8, 9]. Pixel-level annotations for masses, calcifications, axillary findings, and breast tissue, along with tabular clinical data, were validated with high inter-annotator agreement (Cohen's Kappa > 0.95), ensuring reliability (Figure 2 (a-c), Supplementary Table 9, Supplementary Table 6) [11, 29]. Annotating these features required tailored solutions: isodense masses demanded precise boundary adjustments, microcalcifications necessitated iterative calibration for faint clusters, breast tissue required fuzziness threshold tuning, and axillary findings were cross-validated with clinical data [33, 34, 37].

OncoVision's web application enables real-time diagnostic support, integrating seamlessly into clinical workflows to generate structured, interpretable reports that enhance radiologist decision-making and serve as a learning tool for medical students. The pipeline excels in detecting challenging isodense masses and accurately categorizing BI-RADS 4 and 5 cases—critical for identifying high-risk patients—as validated by reader studies showing superior performance over junior radiologists (Extended Data Fig. 8). In resource-limited regions, where expert radiologists are scarce, OncoVision's deployment significantly improves diagnostic access, reducing disparities [12]. By enabling timely detection and management, it promotes equitable healthcare and has the potential to improve patient outcomes globally.

2 Results

We present a comprehensive evaluation of the OncoVision Multimodal Pipeline, a novel end-to-end deep learning framework designed to replicate the structured diagnostic reasoning of expert radiologists in breast cancer assessment from mammographic imaging. OncoVision integrates multimodal inputs, including raw pixel data and derived segmentation masks, through a late fusion architecture to simultaneously segment four anatomically distinct regions—mass, calcification, axilla findings, and breast tissue—and predict ten clinically relevant diagnostic features, culminating in BI-RADS category assignment. The pipeline combines a high-capacity convolutional segmentation backbone with late-fusion modules for structured clinical feature prediction, enabling unified pixel-level and tabular-level reasoning. As illustrated in Fig. 1, this architecture generates standardized, report-ready outputs directly from input images, supporting clinical decision-making in both screening and diagnostic workflows.

OncoVision shows a clear edge over the state-of-the-art UNet++ baseline, which is also extensively used in mammography segmentation [38], in terms of all segmentation metrics across the four ROIs (P < 0.001, Cohen's d = -0.877 for calcification), as measured by Table 1 and Fig. 3a. For mass segmentation OncoVision achieves intersection over union (IoU) of 0.9125 and Dice Similarity Coefficient (DSC) value of 0.9522 as opposed to 0.8785 and 0.9353 for UNet++ which was statistically significant with P - value < 0.001, Cohen's d = -0.346 for IoU (Extended Data Table 4). The significance of such improvements are clear in the context of malignant mass, as accurate boundary detection is important for surgical planning and biopsy. For the calcifications, a difficult ROI because of their small size and low contrast, OncoVision results in 0.7351 IoU and 0.8413 DSC which are higher than UNet ++'s performance (IoU 0.6485 and DSC 0.7868) with p-value below 0.001 and d = -0.849. OncoVision's clinical utility is further demonstrated by its improved sensitivity for microcalcifications, which are frequently an indication of ductal carcinoma in situ (DCIS). Axilla findings, which are vital for lymph node staging, show similar benefits with an IoU

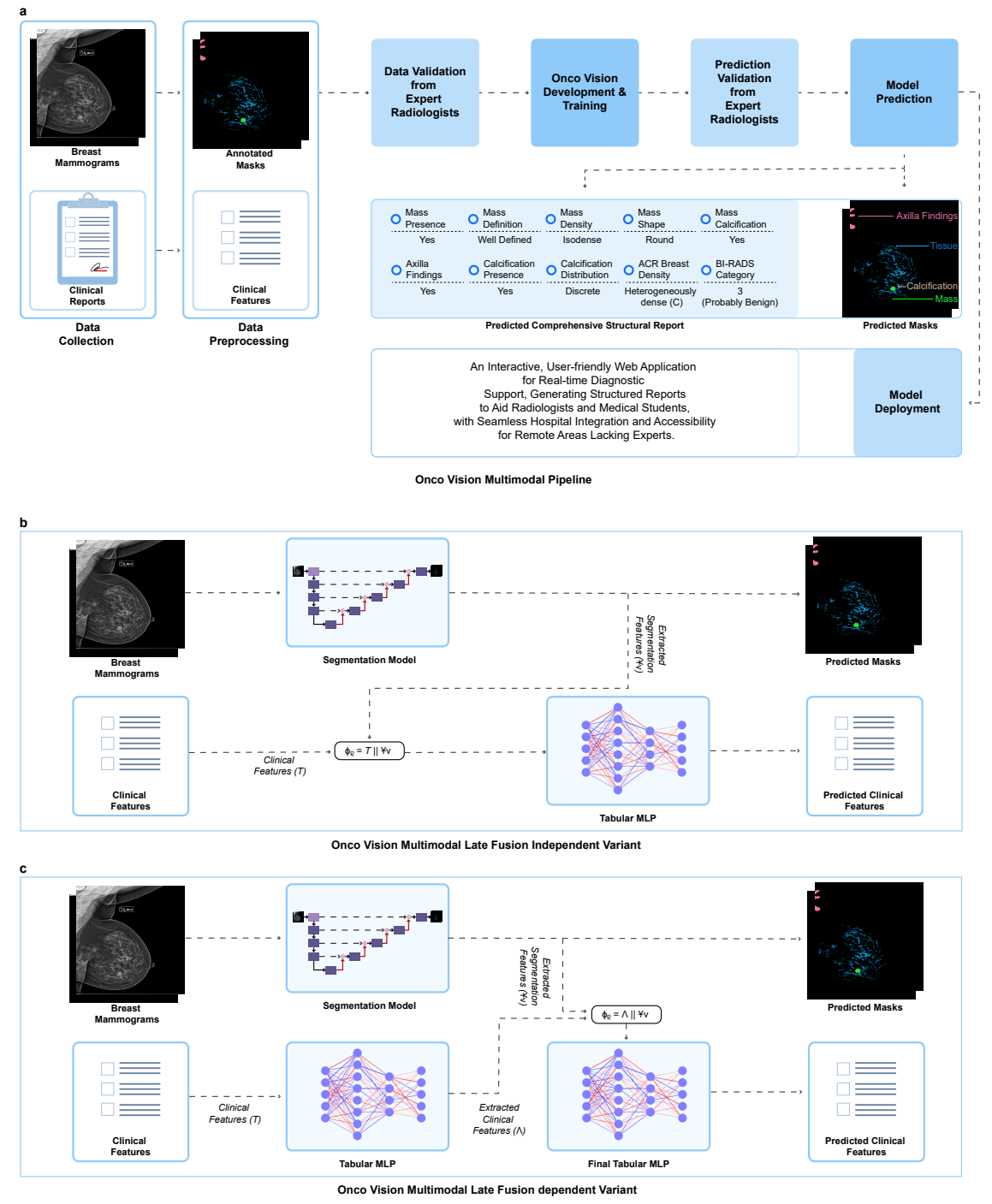


Fig. 1: Integrated workflow and multimodal architecture of OncoVision. (a) End-to-end workflow from data acquisition and preprocessing to model training, evaluation, and web deployment. (b) Late fusion independent variant: segmentation bottleneck features feed directly into an MLP for clinical feature prediction. (c) Late fusion dependent variant: parallel processing of imaging and tabular data, followed by fusion and MLP prediction.

of 0.7839 versus 0.7413 in UNet++, p-value below 0.001 and d = -0.234; breast tissue segmentation features the lowest relative improvement with an IoU of 0.6565 compared to UNet++'s 0.6138, p-value below 0.001 and d = -0.857 due probably also to its large but visually simple structure.

The error map analysis, plotted in Fig. 2 (a-c), visually demonstrates these quantitative benefits. For mass segmentation on patients P1 and P2, OncoVision eliminates false positives (red) and false negatives (blue) at the margins of lesions; zoomed-in insets at $3-4\times$ magnification demonstrate

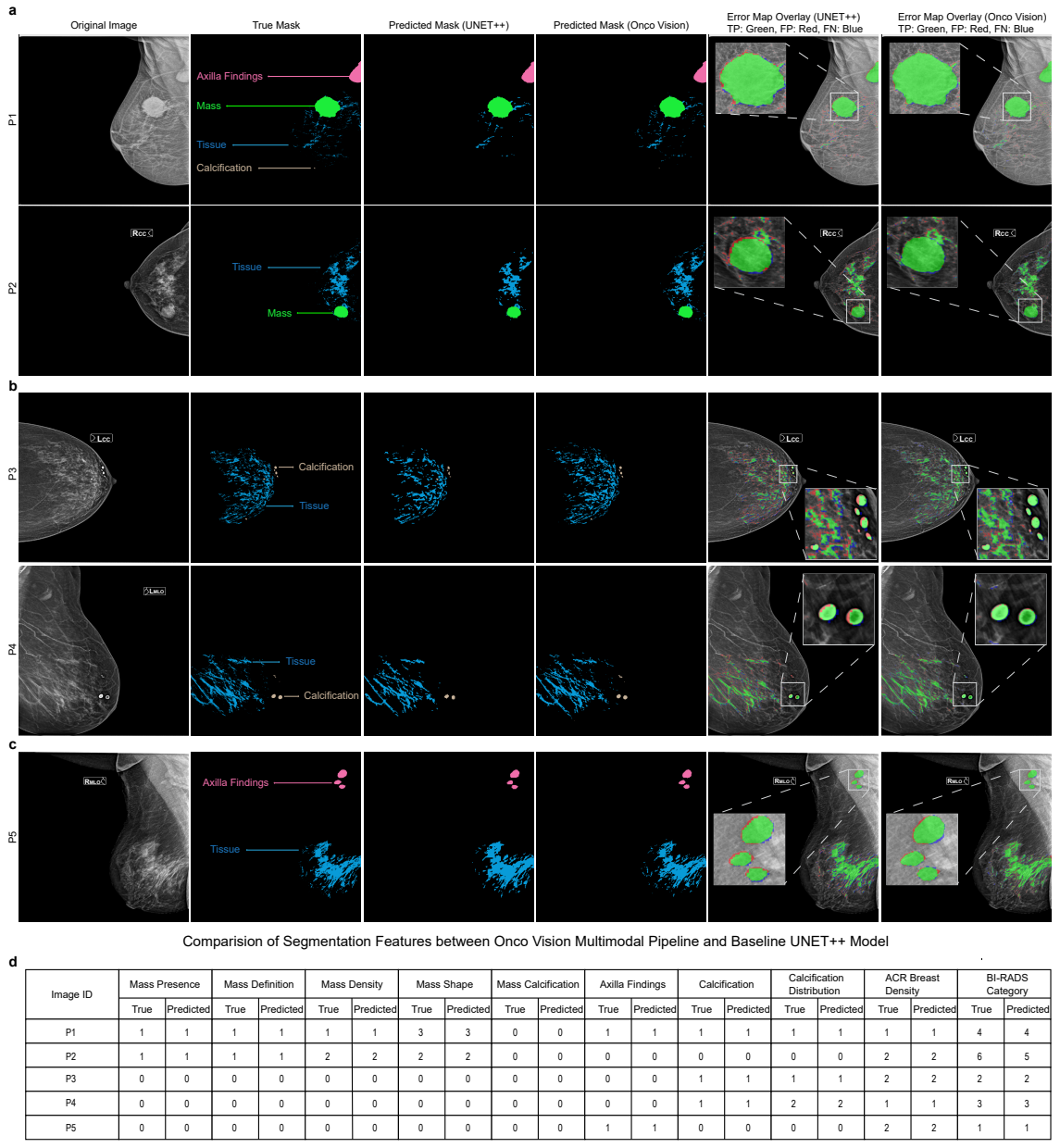
detailed capturing of the densitometric definition of masses in P2, as presented in Fig. 2a. For the two patients P3 and P4 containing calcifications, OncoVision reduces false negative errors for low-contrast clusters thus increasing detection of subtle DCIS-related patterns as illustrated in Fig. 2b. In axilla findings and breast tissue for patient P5, it accurately localizes lymph nodes with fewer false positive errors, enhancing staging accuracy, as presented in Fig. 2c. These reductions in segmentation errors demonstrate OncoVision's robustness to imaging heterogeneity, a critical factor in mammography where subtle lesions significantly impact diagnostic outcomes.

Additional metrics, presented in Table 1, validate OncoVision's superiority over the baseline U-Net++ model for breast cancer diagnostics. Hausdorff Distance (HD) and Average Surface Distance (ASD) are adopted to evaluate the segmentation in medical image by quantifying boundary superimpose of predicted and ground truth masks. HD measures the separation of similarly named boundaries, which is key in identifying outliers with respect to lesion localization while ASD computes the average distance among all sets of boundary points, reflecting overall contour precision. For OncoVision, lower HD, 7.8171 vs 10.5253 pixels for mass and ASD 1.0098 vs 1.3192 pixels compared to base line show more consistent border alignment necessary for accurate lesion localisation in mammography experiment applications. The relative volume difference (RVD) and the relative absolute volume difference (RAVD) show enhanced volumetric agreement, especially for mass with an RVD value of -0.0150.152 versus -0.020.16 benefiting particularly accurate volume reporting in the diagnostic process for DCIS through calcification volume estimation impact. The case is different for the boundary IoU, which has a slightly higher value, e.g., 0.3151 versus 0.2973 on mass, indicating an improvement of edge detection. Statistical tests, presented in Extended Data Table 4, evidence large effect sizes for calcification (d = -0.849 for IoU and -0.877 for DSC) and breast tissue (d = -0.857 for IoU), all with p < 0.001, demonstrating the consistent superiority of OncoVision against the baseline.

OncoVision's late fusion independent variant accurately predicts ten clinical features, producing structured diagnostic reports that align closely with ground truth labels, as shown in Fig. 2d, Table 2, and Extended Data Fig. 10. For patients P1 through P5, predictions match ground truth for all features except P2's BI-RADS category, which is downgraded from 6 to 5, a non-actionable change, demonstrating high concordance critical for clinical decision support, as depicted in Fig. 2d. Table 2 details classification performance across both late fusion variants. The independent variant excels in binary tasks, achieving accuracies of 0.938992 for mass presence and 0.962865 for mass calcification, with F1 scores of 0.946636 and 0.979136, respectively. For multi-class tasks, performance varies by class complexity. For mass definition, the independent variant's F1 score is 0.949192 for the absent class but drops to 0.625 for the spiculated class with a recall of 0.454545, reflecting challenges with rare, morphologically complex classes. Likewise, for BI-RADS, F1 scores ranging between 0.763158 for category 1 down to the lowest recall categories of 5 at only 0.555556 and 6 at only a recall of 0.59375 suggest challenges with imbalanced high-risk classes.

The dependent variant reports slightly lower accuracies (e.g., 0.93634) for mass presence compared to 0.938992 by the independent variant in Table 2) but more precise values on some categories, such as the mass calcification category (0.974026 for this dependent variant versus 0.958333 of the independent one), implicating a more cautious manner to make predictions that may decrease false positives during clinical practical application. For mass shape, the dependent version's F1-score for irregular is 0.781457 versus 0.810811 for the independent version (Table 2), which highlights a compromise of complex morphology treatment. For ACR breast density, the independent variant achieves an F1 score of 0.84 for the heterogeneously dense class compared to 0.761905 for the dependent variant, indicating better performance in challenging dense tissue classifications.

Receiver Operating Characteristic (ROC) analysis, detailed in Extended Data Fig. 10 and Extended Data Table 5, quantifies discriminative performance of OncoVision's independent variant. The independent variant achieves mean AUCs of at least 0.91 across all ten clinical features, with peaks for mass calcification at 0.979 with a 95% confidence interval of 0.972 to 0.985, axilla findings at 0.978 with a 95% confidence interval of 0.97 to 0.985, and calcification distribution for the line/segmental class at 0.991 with a 95% confidence interval of 0.985 to 0.995, as reported in Extended Data Table 5. Additional metrics from Extended Data Table 5 highlight strong performance for mass presence at 0.976 with a 95% confidence interval of 0.968 to 0.983, mass definition with a mean AUC of 0.949 including 0.927 for spiculated masses, mass shape with a mean AUC



Prediction of Clinical Features using Onco Vision Multimodal Pipeline in Late Fusion Independent Variant

Fig. 2: Comparative segmentation and diagnostic profiling using the OncoVision multimodal pipeline. (a–c) Side-by-side segmentation comparison of baseline UNet⁺⁺ and OncoVision across mass (a), calcification (b), and axilla findings with breast tissue (c). Panels show, from left to right: original mammogram, ground truth, UNet⁺⁺ prediction, OncoVision prediction, UNet⁺⁺ error map, and OncoVision error map (true positives in green, false positives in red, false negatives in blue). Zoomed insets $(3-4\times)$ highlight improved boundary delineation and reduced false errors by OncoVision in challenging regions. (d) Clinical feature predictions by OncoVision late fusion (independent variant) for five patients, including mass morphology, axilla findings, calcification distribution, ACR breast density, and BI-RADS category. All predictions match ground truth except one BI-RADS downgrade (P2: $6 \rightarrow 5$). Data are from 345 test mammograms. Error maps show pixel-level differences. No statistical tests applied.

of 0.938 including 0.939 for irregular shapes, and ACR breast density with a mean AUC of 0.921 including 0.967 for highly dense tissue. For BI-RADS, AUCs range from 0.89 for category 2 to 0.941 for category 4, with narrow confidence intervals, for instance, a mean AUC of 0.91 with a 95% confidence interval of 0.898 to 0.921, confirming statistical reliability across the test set with

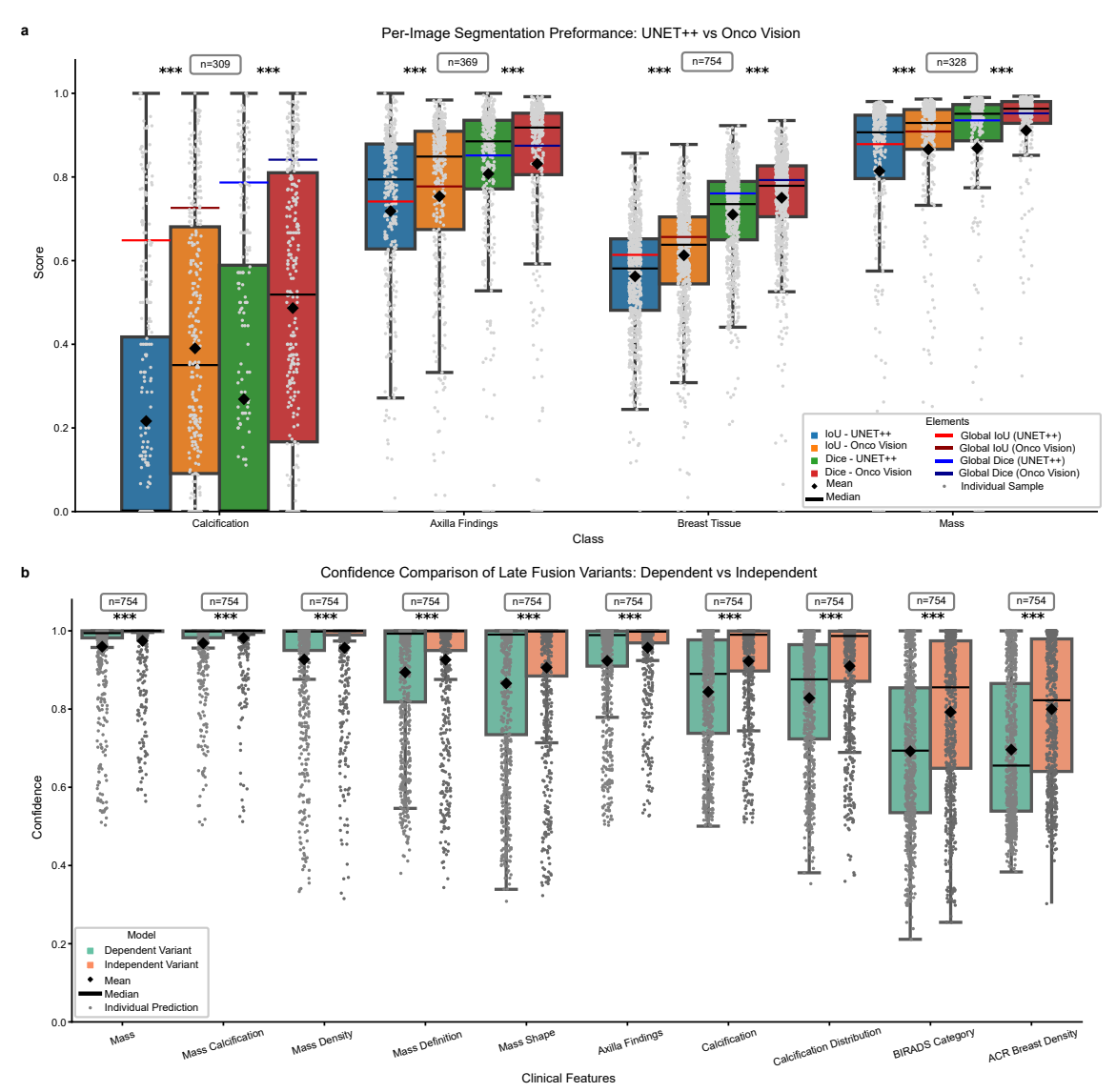


Fig. 3: Comparative per-image segmentation and clinical feature confidence of UNet++ and OncoVision. (a) Box plots of per-image IoU and DSC for calcification (n=309), axilla findings (n=369), breast tissue (n=754), and mass (n=328). Boxes show interquartile range (25th–75th percentile), median (black line), mean (black diamond), and individual scores (gray dots, jittered). Red dashed/solid lines: UNet++ global IoU/DSC; blue dashed/solid lines: OncoVision. Wilcoxon signed-rank test; ***P < 0.001; **P < 0.01; **P < 0.05. Large effect sizes for calcification (DSC: Cohen's d=-0.877) and breast tissue (IoU: d=-0.857). (b) Box plots of model confidence across ten clinical features (n=754 each). Green: dependent fusion; orange: independent fusion. Same box plot conventions. Wilcoxon signed-rank test with Bonferroni correction (adjusted $\alpha=0.005$); ***P < 0.001; **P < 0.01; **P < 0.05. Independent variant shows higher confidence across all tasks.

754 samples per feature. These high AUCs, particularly for categories 4 and 5 at 0.927 with a 95% confidence interval of 0.91 to 0.942, validate OncoVision's ability to support risk stratification, crucial for identifying actionable findings in mammography.

Radiomic features extracted from segmentation outputs provide quantitative biomarkers linked to clinical outcomes, enhancing OncoVision's diagnostic interpretability, as shown in Fig. 5. A heatmap of the top 20 radiomic features, depicted in Fig. 5a, reveals strong correlations above 0.80, highlighted in red, among calcification first-order statistics, including Mean Absolute Deviation,

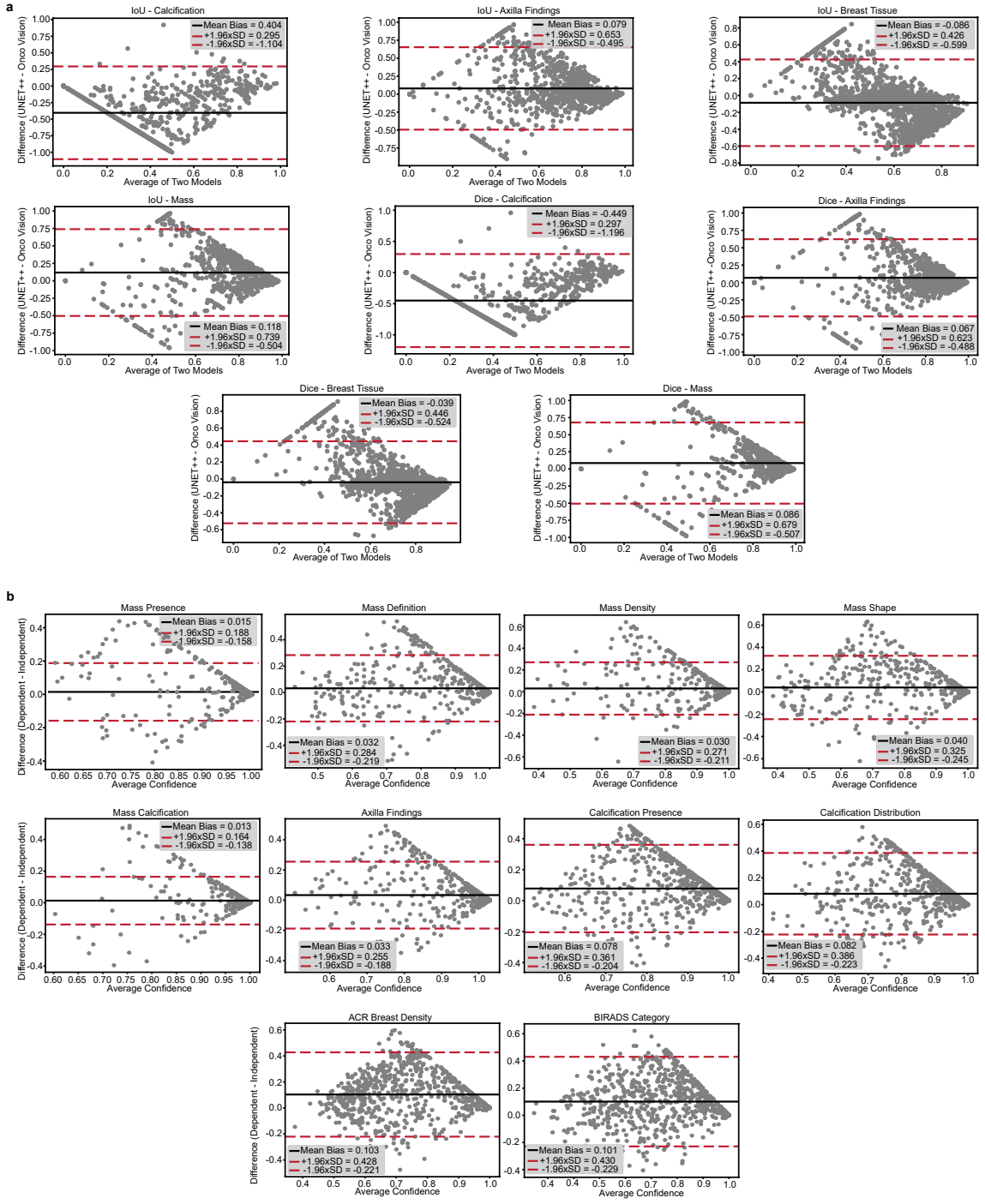


Fig. 4: Bland–Altman analysis of segmentation and confidence performance. (a) Bland–Altman plots comparing per-instance IoU and DSC between UNet⁺⁺ and OncoVision for calcification, axilla findings, breast tissue, and mass (n=309–754 per class). Difference (UNet⁺⁺ – OncoVision) versus average; solid black line, mean bias (-0.449 to 0.118 for DSC); dashed gray lines, 95% limits of agreement (mean $\pm 1.96 \times \text{SD}$, spanning up to [-1.2, 0.3]). Points show individual image differences. OncoVision exhibits positive bias in mass and axilla findings. (b) Bland–Altman plots comparing confidence scores between late fusion independent and dependent variants for ten clinical features (n=754 each). Difference (independent – dependent) versus average; mean bias 0.015–0.104, largest for BI-RADS (0.101) and ACR breast density (0.104); limits of agreement within ± 0.45 . Points show per-instance differences. Independent variant consistently higher.

Range, Variance, and 90th Percentile, reflecting consistent signal heterogeneity in suspicious clusters associated with malignancy. Also grouping together are shape-based features which demostrate similar morphological patterns across ROIs, that is — Mass Shape 2D Perimeter Surface Ratio and Tissue Shape 2D Sphericity. These clusters validate the biological coherence of OncoVision feature extraction, indicating that it captures clinically important patterns.

A bar graph, presented in Fig. 5b, we showed absolute correlations between the top 10 radiomic features and BI-RADS categories in the ranking of from Tissue Shape 2D Maximum Diameter which has the smallest to Mass Shape 2D Perimeter Surface Ratio with largest correlation. The first-order calcification features with the most prominent correlation are Variance, Range and Robust Mean Absolute Deviation, indicating they may be of predictive value in assessing risk of malignancy. Kernel Density Estimation (KDE) plots are shown in Fig. 5c, for five example features (first-order mean, sphericity, kurtosis, total energy and pixel surface) across an axilla finding stratified by BI-RADS with category 1 in blue and category 6 in pink, show systematic distributional differences. The fact that masses with higher kurtosis and total energy are associated with BI-RADS categories 4–6 implies the accentuated complexity in intensity when the masse classified as malignant. Axilla findings have decreased sphericity, which indicates irregular morphology of the malignant lymph nodes, and increased pixel surface in calcifications may indicate segmental or linear patterns - two of the characteristic features of DCIS. These reproducible patterns show that radiomic features encode clinically relevant data not yet perceived by the human eye, contributing to risk stratification and diagnostic considerations.

Bland-Altman analysis, shown in Fig. 4 and detailed in Extended Data Table 3, quantifies agreement between models for both segmentation and clinical feature prediction. For segmentation, OncoVision exhibits a positive bias in mass IoU of +0.1178 and DSC of +0.086, with narrow limits of agreement from -0.504 to 0.7396 for IoU, indicating superior overlap accuracy, as depicted in Fig. 4a. Calcification segmentation shows the largest improvement with an IoU bias of -0.4041 and DSC bias of -0.4494, with limits of agreement from -1.1041 to 0.2958, reflecting enhanced sensitivity to subtle, low-contrast lesions critical for early ductal carcinoma in situ (DCIS) detection. Breast tissue segmentation has minimal bias of -0.0863 for IoU, consistent with its simpler structure, while axilla findings show moderate improvement with an IoU bias of +0.0792. All comparisons are statistically significant with p-values below 0.001, as detailed in Extended Table 4, with large effect sizes for calcification, with Cohen's d = -0.849 for IoU and -0.877 for DSC, and for breast tissue, with d = -0.857 for IoU, confirming OncoVision's consistent superiority over the baseline UNet++ model.

Bland-Altman plots, shown in Fig. 4b, compare confidence scores between late fusion variants for clinical feature prediction. The independent variant produces higher confidence across all tasks, with mean differences ranging from 0.0148 to 0.1035, and the largest bias observed in BI-RADS at 0.1008 and ACR breast density at 0.1035. Limits of agreement remain tight, for instance, ± 0.4307 for BI-RADS, suggesting consistent reasoning despite architectural differences. Small mean differences, such as 0.0148 for mass presence with a 95% confidence interval of 0.0085 to 0.0212, and narrow confidence intervals indicate high agreement, particularly for binary tasks. Higher variability in calcification presence and BI-RADS, with limits of agreement up to ± 0.43 , reflects inherent uncertainty in subjective or low-contrast features, yet the consistent directionality supports the robustness of OncoVision's fusion strategy.

To assess OncoVision's clinical utility, a reader study compared its performance to six radiologists (two juniors, 1–5 years experience; two seniors, 8–10 years; two experts, 15–25 years) across 100 mammographic cases, evaluating diagnostic confidence, time efficiency, and segmentation accuracy (see, Reader Study 4.3, for details). OncoVision achieved a mean confidence score of 0.871 ± 0.077 across ten clinical features (e.g., mass presence, BI-RADS category), surpassing juniors (0.767 ± 0.071 ; 8/10 features, P < 0.001, Cohen's d = 0.856-2.289), matching or exceeding seniors in 5/10 features (P < 0.01, d = -1.083 to 1.033), but trailing experts (0.948 ± 0.046 ; 9/10 features, P < 0.05, d = -2.076 to 0.175), as shown in Extended Data Fig. 8a. With AI assistance, confidence increased significantly for juniors ($0.75-0.79 \pm 0.07$ to $0.88-0.91 \pm 0.02$, P < 0.001, d > 1.3) and seniors (0.88 ± 0.06 to $0.92-0.93 \pm 0.02$, P < 0.001, $d \approx 0.7$), but not for experts (P > 0.05), per Extended Data Fig. 8b. Diagnostic time decreased markedly with AI support (Extended Data Fig. 8c). Juniors saved 55-57% (from $38.8-41.5 \pm 3.6-4.0$ min to $17.0-18.6 \pm 1.4-1.7$ min), seniors 54-61% (from $16.5-18.5 \pm 1.4$ min to $6.5-8.5 \pm 1.4-1.5$ min), and experts 18-22%

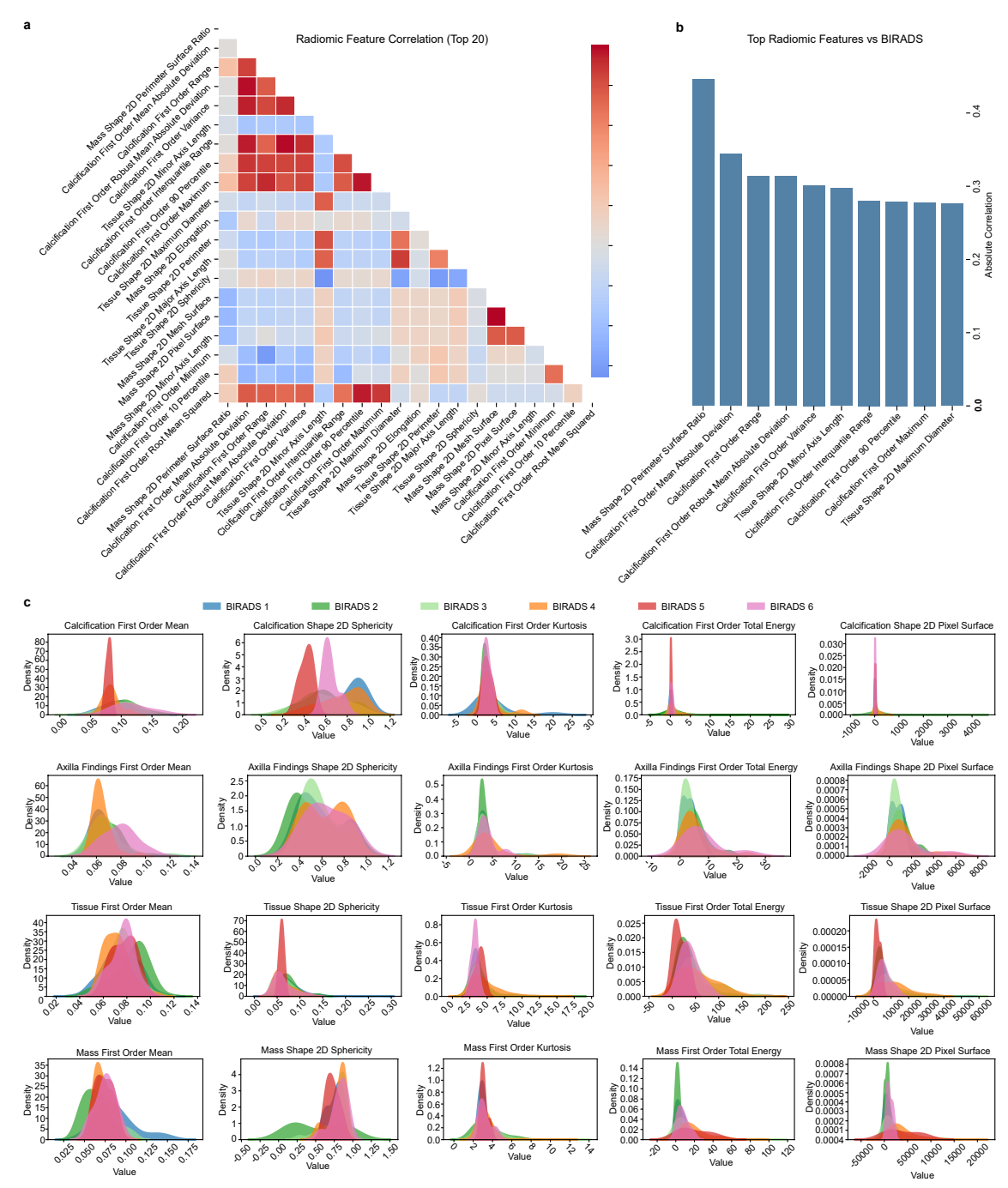


Fig. 5: Radiomic feature analysis and BI-RADS relationships in OncoVision. (a) Heatmap of correlations among the top 20 radiomic features extracted from segmented regions and tabular inputs. Red indicates strong correlations (r > 0.80), orange indicates moderate correlations, and blue indicates weak correlations. (b) Bar plot showing the absolute correlations of the top 10 radiomic features with the BI-RADS category, ordered from lowest (Tissue Shape 2D Maximum Diameter) to highest (Mass Shape 2D Perimeter Surface Ratio). (c) Kernel Density Estimation (KDE) plots of five radiomic features — first-order mean, sphericity, kurtosis, total energy, and pixel surface — for axilla findings, stratified by BI-RADS categories: BI-RADS 1 (blue), BI-RADS 2 (green), BI-RADS 3 (light green), BI-RADS 4 (orange), BI-RADS 5 (light red), and BI-RADS 6 (pink).

(from $7.0-8.0 \pm 1.1-1.2$ min to $5.7-6.3 \pm 0.4$ min), with reduced variability indicating predictable workflows. For segmentation, OncoVision outperformed two radiologists (5–10 years experience)

in mass segmentation (IoU: 0.925 vs. 0.904–0.907, P < 0.001, d = 0.618–0.683), but was slightly less accurate for calcifications (0.720 vs. 0.739–0.740), axilla findings (0.813 vs. 0.823–0.825), and breast tissue (0.659 vs. 0.684; P < 0.001, d = -0.232 to -0.476), as shown in Extended Data Fig. 8d. Segmentation time dropped from \sim 120 min to 10–15 min per batch with AI (Extended Data Fig. 8e). These findings highlight OncoVision's role in enhancing confidence and efficiency for non-expert radiologists while excelling in mass segmentation.

Gradient-weighted Class Activation Mapping (Grad-CAM) visualizations, depicted in Extended Data Fig. 9 (a-d), enhance OncoVision's interpretability by revealing attention patterns across convolutional layers for mass, calcification, axilla findings, and breast tissue segmentation. Early-layer activations focus on coarse localization, mid-layer activations refine feature extraction, and bottleneck-layer activations emphasize precise boundary delineation, with strong activation at lesion margins and internal structures. This incremental refinement is consistent with clinical morphology, which contributes to radiologist trust and emphasizes anatomically meaningful regions. For instance, in the mass segmentation, activations (here or at subsequent location) are focussed on the non-smooth boundary whereas in case of calcifications they focus on clustered pattern which aids diagnostic accuracy.

Examination of failure cases is illustrated in Extended Data Fig. 9e, constrains the ability to detect low contrast microcalcifications that occupy less than 0.1% of area with intensity difference less than 5 Hounsfield Units (HU), a unit of radiodensity defined by subtle grayscale variations in mammography. Zoomed/upscaled insets in 8-10x magnification show clusters missed due to subnoise pixel values, an issue for both AI and human radiologists. Such errors were detected in two cases; however, it emphasizes the requirement of advanced preprocessing or multi-modal input for improving sensitivity for sub-visual lesions, that is known as the bottleneck in mammography.

OncoVision's comprehensive pipeline is including segmentation, clinical feature prediction and radiomic analysis for the development of a robust, interpretable diagnostic tool targeted at breast cancer explanation. The better segmentation performance of it can be seen in Table 1 and Fig. 3a decreases false negatives in crucial regions of interest like calcifications and thus improves early diagnosis of DCIS. Large AUC values of clinical features, as displayed in Extended Data Fig. 10 and Extended Data Table 5, as well as high radiomic-BI-RADS correlations, as shown in Fig. 5, show its potential to produce actionable, concise reports. Statistical validation, presented in Fig. 4 and Extended Data Table 4 to Extended Data Table 3, demonstrates reliability, significant advancements with respect of the baseline UNet++ model as well as consistent performance among fusion variants. Interpretability through Gradient-weighted Class Activation Mapping and failure case analysis demonstrates the merits as well as areas for improvement of OncoVision, which paves the way for deploying an AI system that can potentially complement radiologist workflow in high-stakes mammography setting.

3 Discussion

We present OncoVision, a multimodal AI framework that advances breast cancer diagnosis by simultaneously segmenting four anatomically distinct regions—mass, calcification, axilla findings, and breast tissue—and predicting ten structured clinical features directly from mammographic images. This end-to-end pipeline generates radiologist-interpretable outputs, facilitating seamless integration into clinical workflows.

OncoVision achieves high segmentation performance across all regions. For example, mass segmentation reached an Intersection over Union (IoU) of 0.9125 (Dice = 0.9521), while calcification, axilla findings, and breast tissue achieved IoU scores of 0.7351, 0.7839, and 0.6565, respectively (Table 1). Clinical feature prediction also demonstrated strong results: the late fusion independent variant achieved mean AUCs above 0.91 across tasks, including 0.979 for mass calcification, 0.991 for line/segmental calcification distribution, and 0.941 for BI-RADS category 4 (Table 2). These findings highlight both precision and generalization in complex diagnostic reasoning. The architecture combines a encoder–decoder based backbone with attention gates and dual-path late fusion to integrate imaging-derived bottleneck features with tabular representations. The *independent* variant maps latent segmentation features directly to clinical labels via an MLP, whereas the *dependent* variant models tabular data explicitly through a parallel MLP before fusion. Both approaches significantly outperformed the UNet++ baseline in segmentation (all p < 0.001, Wilcoxon signed-rank

test, Bonferroni-corrected), with the largest gains observed for calcification (Cohen's d = -0.877 for Dice) and breast tissue (d = -0.857 for IoU). This indicates clinically meaningful improvements (Fig. 3).

To our knowledge, OncoVision is the first AI system to perform multi-region segmentation of mass, calcification, axilla findings, and breast tissue within a single framework. Prior studies have addressed isolated tasks such as mass segmentation (IoU ~ 0.91) [39] or calcification detection (AUC = 0.95) [40], but none have jointly modeled these diverse structures. Axillary findings, in particular, remain underexplored in the context of segmentation. To our knowledge, no prior work has specifically performed pixel-wise segmentation of axillary structures in mammograms; existing studies have predominantly focused on classification or detection of axillary lymphadenopathy or fatinfiltrated nodes [41]. Likewise, such a few works have generated spatially resolved tissue masks that achieves around IoU = 0.784 and F-score= 0.911 (for breast-area segmentation in mammograms [42]) which is at pair with the Dice of OncoVision =0.7926 for the same task). OncoVision bridges this gap through precise segmentation and classification, thereby preventing volumetric as well as radiomic assessments. For clinical feature prediction, OncoVision targets a broader class of features than previous models; most other systems have been designed to predict only a small number of features. Previous works have been conducted for mass, such as shape [43] and global calcification, like presence [44]. Other works have studied breast density estimation [42] and BI-RADS categorization of the image, while axilla findings have been analyzed mostly for classification or detection [45]. However, there are no reports on systematic prediction of comprehensive clinical signs and symptoms before. Onco Vision combines all of these different tasks, mass shape, density, definition, calcification presence and type, distribution, breast density, axilla finding and also BI-RADS assessment into a single framework supporting the holistic clinical reading. Robustness across design choices was additionally confirmed through agreement between the fusion variants. Beyond performance, interpretability remains central. Grad-CAM visualizations and dual-confidence reporting (highest and second-highest predictions) support the explainability of clinical reasoning. Examination of failure cases showed limitations in discerning the sub-visual microcalcification (< 3 pixels, $\Delta I < 5$ HU), which continue to be a difficult task even for expert readers [46]. Another restriction is that no architectural distortion is provided in the clinical reports, attaining it could potentially enable the system to better annotate subtle radiological hints. These constraints reflect the fact that OncoVision should be in a decision-support, rather than decision-replacement, role with respect to radiologist expertise. Looking ahead, several opportunities arise. Applying this multimodal concept to other imaging modalities including ultrasound, MRI and PET could extend applicability to a wide range of clinical scenarios, especially in difficult cases where mammography alone is not enough. Integration between modalities could potentially help with longitudinal disease monitoring and more accurate tumor growth, response to therapy and risk of recurrence quantification. Apart from imaging similarly combining with other data types such as genomic and transcriptomic profiles, patient history, electronic health records, and biomarker information offers the potential to form complete patient representations needed for personalized risk assessment, prognostic modeling and therapy decision support. The these approaches may additionally be extended in future work to more difficult imaging patterns like architectural distortion or subtle textural changes that typically remain hidden for traditional radiologic analysis while being clinically relevant as suspected early signs of malignancy. Highly interpretable methods such as counterfactual explanations, prototype-based reasoning and causal inference models might build trust with clinicians and generate actionable insights into the decision mechanism. Both optimization for edge and cloud platform integration are important from a practical point of view as we aim for deployment in real-world scenarios, e.g., healthcare organizations with limited high-end infrastructure. Federated and privacy-preserving learning frameworks can be further developed to support security model training among multi-institutional datasets, while still scalable and patient-privacy preserving.

OncoVision represents a novel approach to breast cancer diagnosis by integrating multi-region segmentation, structured clinical reporting in a holistic-interpretable AI framework. By concurrently segmenting masses, calcifications, axilla findings and breast density - including the prediction of ten diagnostic key features such as BI-RADS category - it provides a step forward from mere isolated task optimization to reasoning in parallel with radiologists. Operated as a secure, user-friendly web application, the system promotes diagnostic standardization of medical education and delivery to underserved areas by providing expert-level interpretation. Our end-to-end pipeline

establishes a new state-of-the-art for multimodal AI in mammography, proving that high accuracy, interpretability and real-world utility can coexist within a clinically deployable tool. With the trajectory of imaging, genomics and longitudinal data intersecting in oncology, platforms like OncoVision will have a major influence on which way equitable precision-driven cancer care goes.

4 Methods

4.1 Dataset Description

4.1.1 Data Collection

The dataset consists of 1,725 mammograms of 500 patients appear to be a diverse and representative sample for generalizable AI performance and was curated from Bangladesh Specialized Hospital Limited (Dhaka, urban) and Khwaja Yunus Ali Medical College & Hospital (Rajshahi, rural). Image quality was checked for high resolution in cranio-caudal (CC), mediolateral oblique (MLO) as well excluding artifacts and demonstrating diagnostic clarity by radiologist review and cross-referencing with electronic medical records (EMR). Clinical data are composed by categorical features: mass presence, mass definition, mass density, mass shape, mass calcification, axillary findings, calcification presence and distribution, ACR breast density, and BI-RADS categories. Fig. 2a–c depict example mammograms, segmentation masks and table of features; Supplementary Table 9 lists feature distributions. Explicit informed consent was waived because of the retrospective nature of the study, and all procedures were in accordance with the ethical standards of both hospitals' Institutional Review Boards (IRBs). The data was de-identified under Health Insurance Portability and Accountability Act (HIPAA) regulations and local rules to maintain privacy.

4.1.2 Data Annotation and Validation

The annotation process was rigorously designed to ensure high-quality, clinically relevant annotations for imaging and tabular data, enabling robust AI model development for OncoVision's mammography pipeline. Segmentation masks for regions of interest (ROIs)—masses, calcifications, axillary findings, and breast tissue—were created with pixel-level precision, adhering to American College of Radiology (ACR) guidelines to ensure consistency and alignment with clinical diagnostic standards (Extended Data Fig. 2). Clinical features, extracted from clinical reports, encompassed categorical features: mass presence (yes, no), mass definition (well-defined, ill-defined, spiculated), mass density (low-dense, isodense, high-dense), mass shape (oval, round, irregular), mass calcification (yes, no), axillary findings (yes, no), calcification presence (yes, no), calcification distribution (discrete, clustered, line/segmental), ACR breast density (fatty/normal, fibroglandular/mixed, heterogeneously dense, highly dense), and BI-RADS categories (1-6) (Supplementary Table 9, Supplementary Table 7). Both, mask and features were validated by two expert radiologists through careful visual inspection, consensus meetings to resolve discrepancies, and comparison with EMR including troubleshooting of isodense masses embedded in normal tissue or faint microcalcifications (<0. 1\% of image area) (Extended Data Fig. 11, Extended Data Fig. 12). We obtained high interannotator agreement (average Cohen's $\kappa = 0.97 \pm 0.01$, Fig. 5) after consensus annotation. Fig. 6e-f demonstrated the reliability of the dataset in different clinical scenarios and made it appropriate for training and testing OncoVision's segmentation and diagnostic applications, especially for settings where consistency diagnosis is significant like low resource regions.

4.1.3 Data Preprocessing

Normalization and standardization of both imaging and clinical data was carefully applied to guarantee robust performance of OncoVision. Such preprocessing was necessary to reduce variability in data distribution, improve model convergence and increase generalizability between different clinical settings as illustrated in Fig. 2a and Extended Data Fig. 12. Through resolving problems, such as nonuniform pixel intensities in mammograms or diverse scales of tabular features, these methods innovatively paved the way for successful multimodal fusion and robust predictions. In the imaging dataset, mammography images were normalized to consolidate pixel intensities and to guarantee a homogeneous input for the segmentation model. The normalization process was applied along the

image channels using z-score normalization, as described by the formula:

$$\iota_{\nu} = \frac{\iota - \mu}{\sigma},\tag{1}$$

where ι denotes the raw pixel intensity values, μ represents the dataset mean intensity, σ is the standard deviation, and ν indicates the normalized intensity representation. This transformation standardizes the pixel values to have a mean of zero and unit variance, reducing differences between imaging devices or acquisition protocols, and enabling the convolutional Neural Network (CNN) to concentrate on medical structures rather than artifacts, as visually illustrated in Fig. 1(b-c) and Extended Data Fig. 7. Segmentation masks were preprocessed to encode categorical labels corresponding to different anatomical and pathological structures, such as masses, calcifications, and breast tissue. Each RGB mask was first label-encoded into integer class labels, followed by one-hot encoding to prepare the ground truth for multi-class segmentation tasks. Mathematically, the one-hot encoding process can be expressed as:

$$\eta_{\xi}[i, j, \omega] = \begin{cases} 1, & \text{if } \eta[i, j] = \omega, \\ 0, & \text{otherwise,} \end{cases}$$
(2)

where η represents the label-encoded segmentation mask, ω is the class index, and η_{ξ} denotes the one-hot encoded mask with dimensions (H,W,ω) , where H and W are the spatial dimensions of the mask and ω is the total number of classes. This encoding ensures that the model receives unambiguous categorical targets for training.

For the categorical features, no missing values were observed for key features such as mass presence, mass definition, mass density, and BI-RADS category. Completeness was ensured through structured clinical reports and cross-referencing with with the original dataset, as shown in Supplementary Table 8. Preprocessing challenges from ambiguous mammography images, especially isodense masses and microcalcifications, were addressed through radiologist-guided annotation (Fig. 2a-c, Extended Data Fig. 9e). The isodense masses, which were not with contrast of surrounded tissue, needed repeated brightness, contrast and curve adjustments under the guidance of expert to achieve delineation (Extended Data Fig. 11). Mask analysis demonstrated low variability and good reproducibility (Supplementary Table 6). Microcalcifications fainter and more variable were refined from radiologist feedback, resulting in enhanced detection and inter-annotator agreement in disperse or cluster cases (Fig. 2b, Extended Data Fig. 12, Supplementary Table 7). Axillary outcomes were routine, whereas Fuzzy threshold of breast became tricky to set appropriately. Radiologist validation improved the accuracy and contour precision (Fig. 6a, Fig. 2c, Extended Data Fig. 13). Some continuous features, including patient age and mass size, were removed from model input when trained to retain discriminative variables and reduce the complexity of the input space (Supplementary Table 9, Supplementary Table 8). Mass size was instead extracted after training from the predicted segmentation masks, as a means of keeping it aligned with model outputs; results in good likelihood to ground truth along with low error (Fig. 2). Patient age, which has limited predictive power for segmentation and feature prediction, was retained for downstream tasks such as risk stratification and treatment planning. This selective exclusion rationalizes training yet maintains clinical utility and flexibility for secondary analyses (Extended Data Fig. 12-Extended Data Fig. 13). To tackle the issue of class imbalance, we performed specialized data augmentation based on categorical feature ratios derived from medical reports (mass present, morphology, calcification patterns and BI-RADS categories (Supplementary Table 9, Supplementary Table 6). The original 1,725-case dataset had a severe class imbalance for malignancy (BI-RADS 4: 5.7%, BI-RADS 5: 1.0%), spiculated (0.5%) and high-density masses (2.7%), clustered microcalcifications (2.1%) and highly dense breasts (3.7%) (Supplementary Table 6, Supplementary Table 7). Augmentation prioritized these clinically critical categories to prevent bias toward benign predictions and improve detection of subtle abnormalities (Fig. 6a,b, Extended Data Fig. 12). Post-augmentation evaluation indicated balanced class representation and improvement in model sensitivity and generalization capability across a broad range of tissue types and diagnostic criteria (Supplementary Table 8, Fig. 2). The augmentation was strategically applied to images and tabular features in a way maintaining one-to-one correspondence between ROIs and metadata (Fig. 6). The methodical use of data augmentation is also practiced techniques—rotation, flipping, intensity scaling and

controlled noise injection targeting to fill underrepresented classes. After augmentation, the categorical distributions were more balanced (Fig. 6c, Extended Data Fig. 13) minimizing skewness and improving inter-class fairness. This approach facilitated better capture of clinically important abnormalities and a successful AI prediction in a variety of populations and imaging scenarios.

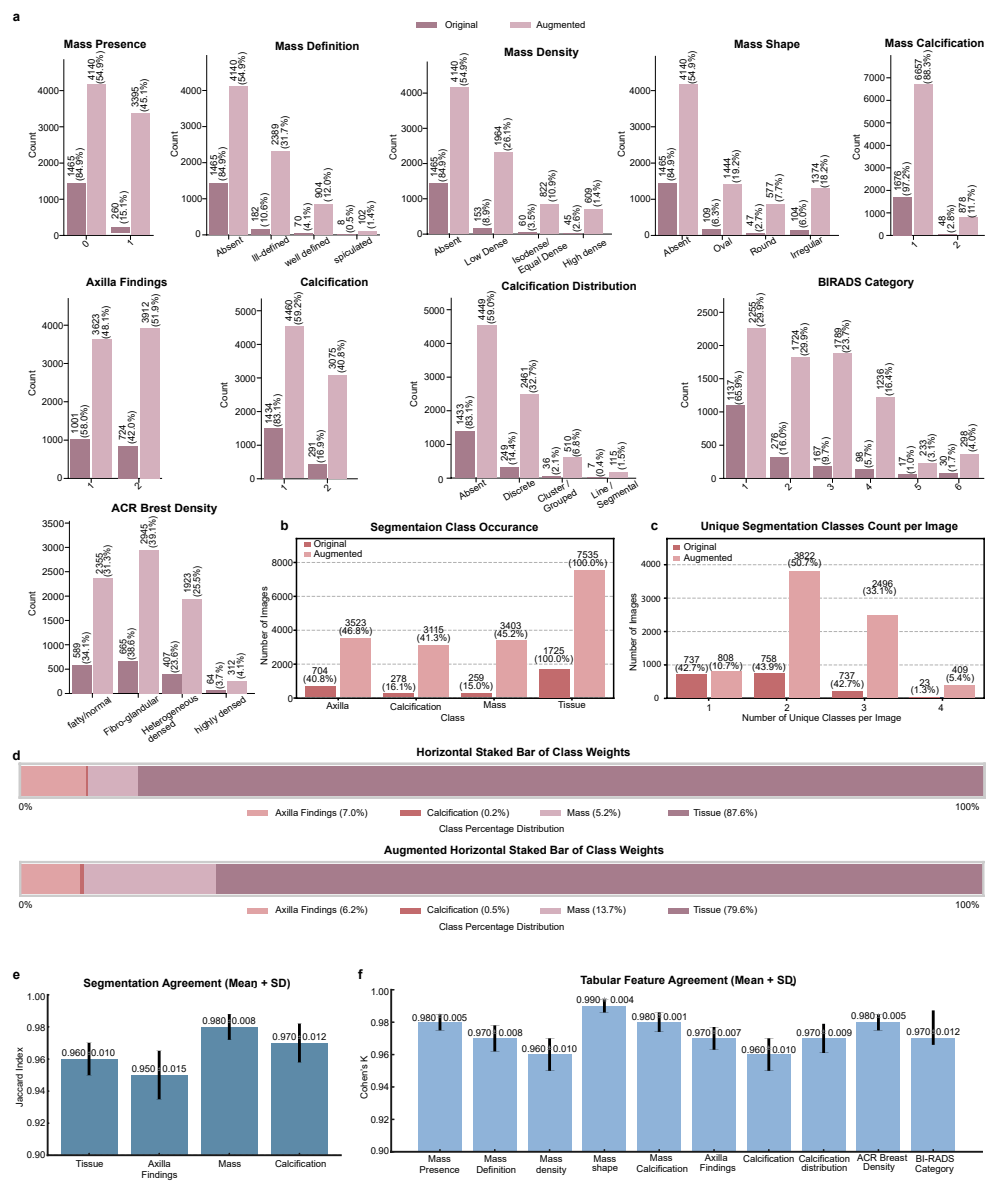


Fig. 6: Pre- and post-augmentation distributional balance and inter-annotator agreement. (a) Class counts and percentages for ten clinical features before and after augmentation, showing improved representation of minority classes such as Mass Definition, Calcification Presence, and BI-RADS Category. (b) Bar plot of segmentation class frequencies across four anatomical regions (Calcification, Axilla Findings, Mass, and Tissue) before and after augmentation. (c) Barplot of unique non-background segmentation classes per image, pre- and post-augmentation, indicating increased multi-class co-occurrence. (d) Stacked horizontal bars of class-weight composition in segmentation masks before and after augmentation, showing redistribution toward balanced representation (e.g., Mass: 5.2% to 13.7%; Calcification: 0.2% to 0.5%). (e) Mean Jaccard index with standard deviation for inter-annotator segmentation agreement: Tissue (0.96 \pm 0.010), Axilla Findings (0.95 \pm 0.015), Mass (0.98 \pm 0.008), and Calcification (0.97 \pm 0.012). (f) Mean Cohen's with standard deviation for clinical feature annotation agreement across ten diagnostic tasks, ranging from 0.96 \pm 0.010 to 0.99 \pm 0.004.

Multimodal augmentation strengthened image-metadata correlations (Supplementary Table 9). Feature distributions by BI-RADS categories were analyzed before and after augmentation (Supplementary Table 6-Supplementary Table 9, Supplementary Table 6-Supplementary Table 8; Fig. 2-Fig. 6, Extended Data Fig. 13c-Extended Data Fig. 7). Mass morphology (well-defined, illdefined, spiculated) showed marked underrepresentation in BI-RADS 4-5 pre-augmentation (e.g., well-defined: < 1%; spiculated: 0.5% overall, < 0.1% in BI-RADS 5). Post-augmentation, welldefined masses rose to 5% in BI-RADS 4, ill-defined to 3% in BI-RADS 5, and spiculated to 1.4% in BI-RADS 5 (Fig. 6a,b, Extended Data Fig. 11, Supplementary Table 9, Supplementary Table 7), improving model sensitivity to high-risk phenotypes. Calcifications were classified as discrete, clustered, or linear/segmental; distributions before and after augmentation are shown in Fig. 6 and Extended Data Fig. 12. Pre-augmentation, discrete calcifications were 14.4% overall (< 2% in malignant cases), rising to 3% in BI-RADS 4 post-augmentation; clustered calcifications increased from 2.1% to 1.5% in BI-RADS 5; linear/segmental rose from 0.4% to 1% in BI-RADS 4 and 0.8%in BI-RADS 5 (Supplementary Table 9, Fig. 6a, Extended Data Fig. 11). ACR breast density categories (fatty/normal, fibroglandular/mixed, heterogeneously dense, highly dense) are illustrated in Fig. 6a and Extended Data Fig. 13. Pre-augmentation: fatty/normal 34.1%, fibroglandular/mixed 38.6%, heterogeneously dense 23.6%, highly dense 3.7%. Post-augmentation, malignant representation increased (e.g., fatty/normal $\sim 10\%$ in BI-RADS 4, fibroglandular/mixed $\sim 15\%$ in BI-RADS 5, heterogeneously dense $\sim 20\%$ in BI-RADS 4, highly dense $\sim 5\%$ in BI-RADS 5) (Supplementary Table 9, Fig. 6). Augmentation harmonized regions of interest (ROIs) with tabular features, preserving one-to-one correspondence (Fig. 6b, Supplementary Table 8). The dataset expanded 4.4 times, improving representation of high-risk features and multimodal coherence (Fig. 6b,c, Extended Data Fig. 12). Targeted augmentation corrected imbalances, enhanced model sensitivity to subtle malignant indicators, and supported robust generalization across BI-RADS categories (Fig. 13a).

4.2 Multimodal Framework and Model Architecture

The OncoVision Multimodal Pipeline integrates mammographic imaging and tabular clinical data to enable simultaneous segmentation of anatomical regions and prediction of diagnostic features, addressing key challenges in breast cancer diagnostics (Fig. 1). By integrating imaging-based spatial data and tabular-based clinical context, the pipeline reduces inter-observer variability, improves robustness for resource-constrained settings, and provides interpretable outputs for radiologists to assist decision support. We propose two late fusion models - independent and dependent, which are aimed at achieving the best possible combination between segmentation and tabular based features while predicting accurate structured diagnostic reports with minor dependence to external annotations. The architecture is built using a UNet-based [47] segmentation model and multilayer perceptrons (MLPs) to generate the segmentation masks and clinical feature predictions allowing for end-to-end diagnostic workflows. For clinical use, we implemented the pipeline as a convenient web application to seamlessly integrate in hospital systems and assist real-time diagnosis in clinical practices.

The independent late fusion variant simplifies multimodal integration by using segmentationbased features to predict anatomical masks and clinical features simultaneously, thus avoiding separate training on clinical data at inference time (Fig. 1a). This design increases generalizability, especially in environments which are lacking complete or consistently accurate clinical annotations, and enables scalable implementation through a web-application embedded with hospital systems. The pipeline uses a UNet-like segmentation model trained with pixel-wise annotations from breast tissue, axilla findings, calcifications and masses deciphered by experienced radiologists. High-levelsemantic features are generated from the bottleneck layer (Fig. 7a) based on a feature extractor sub-model. These descriptors provide rich spatial and contextual information, and are then processed by Global Average Pooling (GAP) to reduce the dimensionality and normalize for scaling. The processed features are then input to an MLP (2 hidden layers, 128-64 units) that is trained to predict ten clinical features: mass presence, definition, density, shape, calcification, axilla findings, calcification present and distribution, ACR breast density and BI- RADS category. By concatenating segmentation features directly into raw clinical annotations (T), the variant bypasses dedicated tabular data processing, streamlining the workflow and improving robustness to missing or noisy clinical data. The feature extraction and prediction pipeline of the OncoVision model can

be formalized as follows. For an input mammogram ι , The segmentation backbone extracts a set of bottleneck features, denoted by

$$\Upsilon = \varsigma(\iota),\tag{3}$$

where $\Upsilon \in \mathbb{R}^{H \times W \times C}$ represents the extracted feature map with spatial dimensions H (height), W (width), and C (number of channels). Here, ς denotes the feature extraction function , and ι represents the normalized input image. To obtain a compact spatial representation, these features are subjected to global average pooling (GAP), producing

$$\Upsilon_{\zeta} = \frac{1}{H \times W} \sum_{i=1}^{H} \sum_{j=1}^{W} \Upsilon_{ij}, \tag{4}$$

such that $\Upsilon_{\zeta} \in \mathbb{R}^{C}$ encapsulates the global information of the feature map. Here ζ represents the global average pooling operation that compresses spatial dimensions into a single channel-wise vector representation. The pooled features are then normalized to ensure consistent scaling across dimensions:

$$\Upsilon_{\nu} = \frac{\Upsilon_{\zeta} - \mu}{\sigma},\tag{5}$$

where μ and σ denote the mean and standard deviation of Υ_{ζ} , respectively. Here, Υ_{ν} represents the normalized version of the pooled feature map Υ_{ζ} , ensuring feature consistency and stability across channels. Then, the raw tabular features (T) concatenate with the processed segmentation features Υ_{ν} to form a fused representation:

$$\Phi_o = T \parallel \Upsilon_{\nu}, \tag{6}$$

where Φ denotes the fused feature representation obtained after concatenation, ϱ represents the fused configuration of the feature space, and \parallel defines the concatenation operator that combines features along the channel dimension. Finally, the normalized features Φ_{ϱ} are fed into a multilayer perceptron (MLP) to predict the clinical features:

$$\hat{Y} = \Xi(\Phi_{\varrho}),\tag{7}$$

where \hat{Y} represents the predicted clinical outputs, obtained through the transformation Ξ , which denotes MLP applying softmax activation for multi-class categorical variables and sigmoid activation for binary variables. This formulation provides a concise mathematical description of the end-to-end feature extraction and clinical prediction process. During training, in independent variant, the segmentation backbone learns to generate pixel-level masks, while the ξ maps the bottleneck features (Υ) to raw clinical annotations (T). Mapping the segmentation features with respect to the raw tabular data for each patient, eliminates requirement of distinct tabular processing pipeline. During inference, the whole pipeline is executed serially: the segmentation backbone produces segmentation masks for both anatomical and pathological regions (masses, calcifications, axilla findings and breast tissue). The extracted bottleneck features (Υ) are then fed to the ξ for clinical feature prediction, leading to structured diagnostic reports. This integrated process, depicted in Fig. 1b - Thus, all predictions are expressed based on mammograms alone, such that the model is more easily incorporable into clinical practice than if it were dependent upon tabular information that may be incomplete or missing in some cases.

The late fusion dependent variant learns more from multimodal information, as it allows segmentation and clinical inputs to propagate along independent paths before fusion, preserving detailed interactions between imaging-based and clinical features for better prediction performance and interpretability (Fig. 1c). This architecture directly simulates clinical data, mitigating the issues on annotation diversity and leading to predictive robustness of clinical features even for heterogeneous data sources. The segmentation pathway is a dual of the independent variant. In parallel, a tabular MLP (2 hidden layers, 128-64 units) processes raw tabular data (T) implement a tabular feature extractor sub-model to extract a set of tabular features to capture high level semantic features, denoted by

$$\Lambda = \varsigma(T),\tag{8}$$

These features are GAP-processed and normalized, then concatenated with Υ_{ν} to form a fused representation:

$$\Phi_{\varrho} = (\Lambda \parallel \Upsilon_{\nu}). \tag{9}$$

The concatenated features are fed into a final MLP with three layers of 512, 256, and 128 units; the model is trained to predict clinical outcomes and the generator generates synthesis segmentation masks directly from the segmentation backbone. Such a fusion enhances the model's robustness by exploiting the complementary information between imaging and tabular modality, which helps with dealing complex interactions such as interaction between mass morphology and BI-RADS categories. Thereby integrating spatial information from images with contextual tabular data. The fused representation is then input to the final MLP to produce clinical feature predictions:

$$\hat{Y} = \Xi_{\rho}(\Phi_{\rho}) \tag{10}$$

where Ξ_{ρ} represents the final MLP responsible for mapping the fused feature representation Φ_{ϱ} to the clinical output space. Softmax activation is applied for categorical outputs and sigmoid for binary outputs, ensuring appropriate scaling for different clinical feature types.

Training involves the joint optimization of all components of segmentation model for segmentation, the tabular ξ for feature extraction, and the Ξ_{ρ} for fused predictions, each aligned with the corresponding ground truth annotations. During inference, the process begins with the segmentation model generating segmentation masks and extracting imaging features (Υ). Simultaneously, the tabular ξ processes the clinical data to produce tabular features (Λ). The imaging and tabular representations are subsequently fused and passed through the Ξ_{ρ} to generate clinical feature predictions \hat{Y} , resulting in structured diagnostic reports. This workflow, illustrated in Fig. 1c, at inference time it only needs mammograms and tabular inputs, so that it can be deployed in the hospital systems as a web app to perform real-time analysis.

The independent variant predicts directly from segmentation features clinical data, instead of processing separately two tabular forms, to minimize the dependence on incomplete annotations and increase robustness in a resource poor environment. Applied as a web application, OncoVision produces consistent segmentations masks and clinical predictions from mammography images without the need for additional imaging modalities, enabling real-time diagnostic reporting in radiologist workflow. The dependent variant employs a dedicated MLP for learning tabular attributes (i.e., calcification distribution, and BI-RADS categories) before fusing with segmentation features to achieve state-of-the-art performance under various metrics. This modality separation is beneficial for feature selection explanation, radiologist confidence, and annotation consistency. Both are Hospital Integrated to reduce interobserver variability in medical decision-making and provide structured, actionable reports that promote diagnostics consistency and accessibility to all patients within clinical settings.

4.2.1 Core Models: Segmentation Model and MLP Variants

The core segmentation model employs a encoder–decoder based architecture enhanced with attention gates and batch normalization to improve feature extraction and localization accuracy. It predicts pixel-level masks for key structures in mammography images, including masses, calcifications, axillary findings, and breast tissue (Fig. 7a). The contraction path of the OncoVision extracts hierarchical spatial features through sequential convolutional blocks followed by max-pooling. Each block applies two 3×3 convolutions initialized with Glorot uniform weights, employs Leaky ReLU activation with α set to 0.1 (For negative inputs, the output is 10% of the input value, allowing a small, non-zero gradient to flow backward, mitigating the dying ReLU problem during training), and incorporates batch normalization and dropout to mitigate overfitting. Filter counts progressively increase $(16 \to 32 \to 64 \to 128 \to 256)$ as spatial resolution decreases. Glorot uniform initialization ensures stable gradient flow during training, preventing vanishing or exploding gradients in deep layers, while the Leaky ReLU activation allows small negative gradients, addressing the dying ReLU problem and enhancing stability and convergence for medical imaging tasks characte-

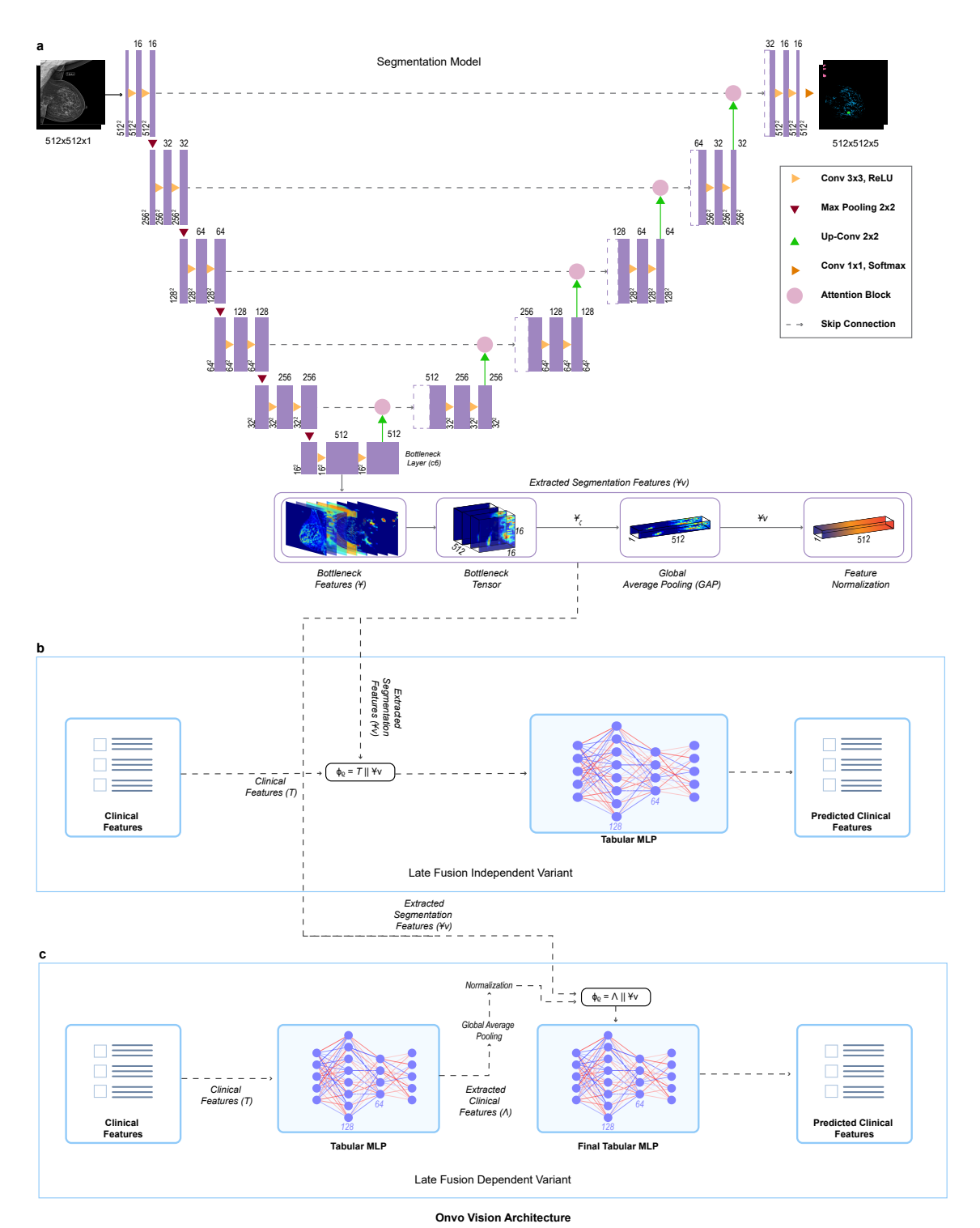


Fig. 7: Detailed architecture of the OncoVision segmentation and late fusion variants. a. The segmentation backbone employs a modified U-Net architecture with encoder—decoder symmetry and integrated attention gates to delineate anatomical and pathological regions in mammograms, including breast tissue, axillary findings, calcifications, and masses. The model outputs multi-class segmentation maps used as structured visual representations for downstream analysis. b. In the independent late fusion variant, the MLP predicts clinical features directly from learned image embeddings, without explicit tabular input. This design enhances generalizability by maintaining predictive alignment with tabular labels while minimizing dependency on incomplete or site-specific metadata. c. In the dependent late fusion variant, tabular and imaging features are processed in parallel through multilayer perceptrons (MLPs) and concatenated at a joint feature space for clinical prediction. This configuration explicitly leverages both modalities, allowing feature-wise interactions between visual and structured clinical data.

rized by high variability [48]. At the network's deepest level, the bottleneck layer utilizes 512 filters to capture high-level semantic representations, serving as the most abstract output of the encoder for downstream clinical feature prediction. The expansive path employs transposed convolutions to recover spatial resolution, with attention gates at each upsampling step refining feature maps by focusing on relevant regions. The attention mechanism operates by processing the skip connection feature map x through a convolutional transformation θ_x and the decoder gating signal g through another convolutional transformation ϕ_g . The resulting feature maps are combined and passed through a ReLU activation to produce an intermediate response f, followed by an additional convolutional operation yielding ψ_f , which refines the spatial attention map guiding the decoder focus. The refined attention map is then given by

$$\tau_x = x \cdot \upsilon(\psi_f),\tag{11}$$

where τ_x denotes the spatially refined feature map obtained by element-wise modulation of x with the attention coefficients $v(\psi_f)$, and $v(\cdot)$ represents the sigmoid activation function, enhancing relevant regions while suppressing background noise. Upsampling blocks continue to use Leaky ReLU for non-linearity and Glorot uniform initialization for weight stability, promoting robust gradient propagation and improving boundary delineation in low-contrast regions such as calcifications. The output layer employs a 1×1 convolution followed by a softmax activation to yield class probabilities:

$$\mathbf{P} = \operatorname{softmax}(\mathbf{W}_{\text{out}} * c_{10} + \mathbf{b}_{\text{out}}), \tag{12}$$

where $\mathbf{P} \in \mathbb{R}^{H \times W \times \omega}$ represents the pixel-wise class probability map, \mathbf{W}_{out} and \mathbf{b}_{out} are the weights and bias of the output convolution, and ω is the total number of segmentation classes (including background, mass, axilla findings, breast tissue and calcification).

The core framework incorporates three MLP variants to support different fusion strategies: one for the independent variant and two for the dependent variant. In the dependent variant, a tabular MLP is used to process raw tabular data (T) and extract high-level feature representations (Λ) for subsequent fusion. The network includes shared dense layers that process the input tabular data T. The input passes through a first dense layer with 128 units and ReLU activation, followed by a dropout layer with a rate of 0.3 to reduce overfitting, and then through a second dense layer with 64 units and ReLU activation. The resulting intermediate representation is mapped to a tabular feature vector denoted by Λ , which encapsulates the learned tabular features extracted from T and serves as the input for subsequent task-specific output heads. Task-specific outputs are obtained through dedicated heads with activation functions chosen according to the number of classes:

$$\hat{Y}[j] = \begin{cases}
\text{Dense}(1, \text{activation} = \text{'linear'})(\Lambda), & \text{if } \omega = 1, \\
\text{Dense}(1, \text{activation} = \text{'sigmoid'})(\Lambda), & \text{if } \omega = 2, \\
\text{Dense}(\omega, \text{activation} = \text{'softmax'})(\Lambda), & \text{otherwise.}
\end{cases}$$
(13)

where $\hat{Y}[j]$ represents the predicted output for the j-th clinical feature, Λ denotes the learned tabular feature vector from shared dense layers, and ω is the number of possible classes for the respective output. Linear activation is used for regression tasks, sigmoid for binary classification, and softmax for multi-class categorical outputs.

In the dependent variant, a final MLP (Ξ_{ρ}) processes fused features by concatenating the segmentation bottleneck features Υ with the tabular features Λ , resulting in

$$\Phi_{\rho} = (\Lambda \parallel \Upsilon_{\nu}), \hat{Y} = \Xi_{\rho}(\Phi_{\rho}) \tag{14}$$

thereby leveraging complementary information from both modalities to improve clinical feature prediction (Fig. 7c).

For the independent variant, a single MLP is used to directly map concatenated raw tabular data and segmentation features to predictions:

$$\Phi_{\rho} = T \parallel \Upsilon_{\nu}, \hat{Y} = \Xi(\Phi_{\rho}) \tag{15}$$

allowing the model to learn joint representations without a separate tabular feature extractor. This design maintains end-to-end inference capability from imaging and tabular inputs while supporting both independent and dependent fusion configurations (Fig. 7b).

The OncoVision Multimodal Pipeline is fine-tuned with a combined loss function that combines segmentation and clinical feature prediction objectives, leading to improved robustness for the dual task. The loss function is a unified form of the Dice and focal losses for segmentation jointly with the categorical cross-entropy regarding clinical feature classification, which was customized designed in view of class imbalance to improve diagnostic accuracy in breast cancer diagnosis.

The total loss for the multimodal pipeline is defined as

$$L_{\mathbf{O}} = \lambda_1 (L_{\mathbf{D}} + L_{\mathbf{F}}) + \lambda_2 L_{\Gamma}, \tag{16}$$

where $L_{\mathbf{D}}$ quantifies segmentation overlap (Dice loss), $L_{\mathbf{F}}$ addresses class imbalance in segmentation tasks (Focal loss), and L_{Γ} measures discrepancies in clinical feature predictions (Cross-Entropy loss). The hyperparameters λ_1 and λ_2 weight the contributions of segmentation and classification losses, respectively.

Dice loss is employed to maximize the overlap between predicted (\hat{M}) and ground truth $(M_{\rm gt})$ segmentation masks, and is formulated as

$$L_{\mathbf{D}} = 1 - \frac{2|\hat{M} \cap M_{\text{gt}}| + \epsilon}{|\hat{M}| + |M_{\text{gt}}| + \epsilon},\tag{17}$$

where small numerical constant, $\epsilon=1\times10^{-5}$ prevents division by zero. This loss emphasizes accurate delineation of small regions such as calcifications. To further address class imbalance in underrepresented regions of interest, including small masses or calcifications, focal loss is incorporated:

$$L_{\mathbf{F}} = -\alpha \sum_{i} (1 - p_i)^{\gamma} \log(p_i), \tag{18}$$

where p_i represents the predicted probability for the true class, balancing coefficient, $\alpha=0.5$ balances contributions from foreground and background, and focusing parameter, $\gamma=2$ focuses training on hard-to-classify pixels, improving sensitivity to subtle lesions crucial for early detection. For clinical feature prediction, categorical cross-entropy loss is used to measure the difference between predicted labels (\hat{Y}) and ground truth annotations (Λ) :

$$L_{\Gamma} = -\sum_{i} \Lambda_{i} \log(\hat{Y}_{i}) \tag{19}$$

which is appropriate for multi-class classification tasks such as BI-RADS categorization. This combined loss formulation ensures that the network jointly optimizes accurate segmentation and reliable clinical feature prediction in a unified end-to-end framework.

The Dice and focal losses for segmentation have been combined to obtain robust boundary delineation in the presence of imbalanced classes, which is important for detecting small clinically significant structures such as microcalcifications associated with DCIS. The hyperparameters ($\alpha=0.5,\,\gamma=2$) of the focal loss have been selected such that to weigh between precision-recall tradeoffs and to prefer challenging areas while not overfitting prominent classes. Categorical crossentropy is well-suited for optimizing clinical feature predictions, favouring structured diagnostic reports. We set hyperparameters $\lambda_1=0.7$ and $\lambda_2=0.3$ (empirically adjusted) for balancing the trade-off between segmentation and classification, which ensure that the model focuses on anatomical accuracy while maintaining clinically trusted predictions. This approach of joint optimization fosters diagnostic consistency, is radiologist centric and enables deployment via a web application for real-time use in clinic and notably under resource limited settings.

4.2.2 Web Application Development

For transitioning from a research prototype, the OncoVision Multimodal Pipeline to a clinical decision-support-system that can be taken up by clinicians, we implemented a secure and responsive web application providing real-time feedback for an end-to-end analysis of mammographic studies. The application is aimed to aid radiologists in diagnostic interpretation, complement training for

under medical students and residents and expand expert-grade disease assessment of breast cancer to underserved or under remote locations where the availability of subspecialty radiologists is scarce.

The web interface of OncoVision allows users to be able to upload an entire bilateral mammographic study (comprising out a cranio-caudal and mediolateral oblique view for both the left(L) and right(R) (e.g., R_CC, L_CC, R_MLO, L_MLO) breast to the system in Digital Imaging and Communications in Medicine (DICOM)- or standard image formats(JPEG/PNG). At submission time, each image is intensity-normalized to a standard scale and resampled to 512×512 pixels before being fed into the OncoVision pipeline, which simultaneously produces high-resolution segmentation masks in four anatomical areas mass (in light green), calcification (in cream), axilla findings (in pink), and breast tissue (in blue) overlaying the original mammography using WebGL-accelerated canvas for swift interactions. Concurrently, the late fusion independent variant predicts ten clinical features per patient, aggregated across views via attention weighting based on image quality and lesion conspicuity, including mass presence (yes/no), definition (well-defined, ill-defined, spiculated), density (low-dense, isodense, high-dense), shape (oval, round, irregular), calcification status (present/absent), axilla findings (positive/negative), calcification distribution (discrete, clustered, line/segmental), American College of Radiology (ACR) breast density (fatty/normal, fibroglandular/mixed, heterogeneously dense, highly dense), and Breast Imaging-Reporting and Data System (BI-RADS) category (1–6), with both top and second-highest confidence scores displayed to support differential diagnosis. Interpretability is enhanced through Gradient-weighted Class Activation Mapping (Grad-CAM) at early, mid, and bottleneck layers, highlighting influential regions such as lesion boundaries and microcalcification clusters, with user-toggleable depth views (Supplementary Fig. 14). All outputs are compiled into a standardized, automatically generated PDF report containing patient-level summaries, confidence scores, segmentation overlays, Grad-CAM visualizations, with final BI-RADS assessment, and metadata (timestamp, model version, disclaimer) for traceability and integration with hospital systems. Running on a Dockerized Ubuntu 20.04 server featuring TLS 1.3 secure communication, it is run by Django (backend), React. js (frontend) and an NVIDIA RTX 3060 GPU with TensorRT optimization (average inference: 1.7 s/image), our platform aims to enable cross-device accessibility, in the frontier of AI by providing actionable, transparent, and auditable diagnostic support that are scalable not just within the context of advanced AI but also into clinical practice even within less-resourced environments.

4.3 Reader study

To investigate the clinical value of OncoVision in real-world diagnosis, a multi-reader, multicase reader study was performed to compare with human radiologists using three critical parameters within diagnostic workflows: diagnostic confidence levels, time efficiency and segmentation accuracy. This study was approved by the IRB, and all subjects gave written, informed consent. Ethical aspects were data anonymization and secure study data handling, as well as prevention of reader fatigue (risk minimization strategies: only 10 cases viewed on a daily basis; reading scheduled over a period of 3 months with flexible deadlines). Six board-certified radiologists were enrolled, with experience stratification including two juniors (1-5 years after residency), two seniors (8-10 years), and two experts (15–25 years). A reference set of 100 retrospectively labeled mammographic cases was chosen from a heterogeneous population with a variety of breast cancer characteristics (benign and malignant, high/low density, simple/complex). Radiologists independently evaluated the case in a blinded fashion and filled out a structured report for the performance of 10 different clinical items: mass presence, definition, density, shape and calcification; axilla findings; calcifications noting its presence and distribution; breast densities according to ACR criteria; and BI-RADS category. For each feature, confidence (0-1 scale, with 1 representing full certainty) was designated by the readers. The time per case was monitored using preconfigured software timers. Subsequently, OncoVision processed the same cases, generating predictions with dualconfidence scores (late fusion dependent and independent variant). In a paired analysis, readers repeated assessments on the same cases with OncoVision assistance, accessing its segmented outputs, predicted features, and visualizations via the web application. Assistance was provided in a decision-support mode, where AI outputs were presented alongside images but final interpretations remained at the reader's discretion. For segmentation evaluation, two additional radiologists (5–10 years experience) manually annotated 100 complex cases (featuring isodense masses, microdiscrete calcifications, and intricate breast tissue structures) with time recorded. These annotations

ROI	↑IoU	↑Dice	†Precision	↑Sensitivity	↑F1 Score	†Specificity	↓HD (px)	↓ASD (px)	†Boundary IoU	$\begin{array}{c} \text{RVD} \\ \text{(mean} \pm \text{std)} \end{array}$	$\begin{array}{c} \text{RAVD} \\ \text{(mean} \pm \text{std)} \end{array}$
						UNet++					
Mass	0.8785	0.9353	0.9423	0.9313	0.9361	0.9794	10.5253	1.3192	0.2973	-0.02 ± 0.16	0.05 ± 0.15
Axilla Findings	0.7413	0.8514	0.8728	0.8356	0.8531	0.9719	25.1785	4.1672	0.2992	-0.04 ± 0.21	0.09 ± 0.18
Breast Tissue	0.6138	0.7607	0.7854	0.7386	0.7615	0.9457	55.2629	2.0713	0.3222	$+0.01 \pm 0.42$	0.21 ± 0.37
Calcification	0.6485	0.7868	0.8217	0.7561	0.7877	0.9811	95.0511	18.7892	0.2103	-0.22 ± 0.39	0.25 ± 0.36
					(OncoVision					
Mass	0.9125	0.9521	0.9622	0.9424	0.9522	0.9881	7.8171	1.0098	0.3151	-0.015 ± 0.152	0.041 ± 0.147
Axilla Findings	0.7839	0.8747	0.9020	0.8491	0.8747	0.9752	20.6907	3.5071	0.3188	-0.035 ± 0.204	0.080 ± 0.191
Breast Tissue	0.6565	0.7926	0.8145	0.7720	0.7927	0.9541	45.0871	1.5258	0.3525	$+0.007 \pm 0.410$	0.190 ± 0.364
Calcification	0.7351	0.8413	0.8923	0.7959	0.8413	0.9845	83.3120	15.5355	0.2361	-0.200 ± 0.379	0.236 ± 0.357

Table 1: Comprehensive quantitative comparison of segmentation performance between Baseline and OncoVision across multiple regions of interest (ROIs) and evaluation metrics. Table shows a comprehensive comparative analysis of performance of the baseline UNet++ model and the proposed OncoVision framework which exploits fusion of multimodal data and attention mechanisms for glandular segmentation. Experimental results are presented on four clinical ROIs: Mass, Axilla Findings, Breast Tissue, and Calcification. Comparison is conducted with standardized quantitative metrics including Intersection over Union (IoU), Dice Similarity Coefficient (Dice), Precision, Sensitivity, F1 Score, Specificity, Hausdorff Distance (HD) in pixels, Average Surface Distance (ASD) in pixels, Boundary IoU and Relative Volume Difference (RVD) and, Relative Absolute Volume Difference (RAVD). OncoVision achieves more reliable performance than UNet++ on most metrics and ROIs, where improvements in IoU and Dice (and decreases in HD and ASD, meaning tighter boundary fitting) and better volumetric consistency are observed in terms of RVD-AVD (reported as mean \pm standard deviation). The positive and negative (\uparrow) and (\downarrow) signs indicate whether the larger or smaller value is preferred. Bold indicates the bestperformer scores OncoVision makes consistent gains across all tasks, especially for difficult tasks e.g., Calcification segmentation or complex structures e.g., Mass.

were compared to OncoVision's automated segmentations for four regions of interest (ROIs): masses, calcifications, axilla findings, and breast tissue. Statistical analyses were performed using Python. Confidence scores and times were compared using Wilcoxon signed-rank tests (paired for with/without AI; unpaired for group comparisons), with one-tailed tests for expected AI improvements and Bonferroni correction for multiple comparisons where applicable ($\alpha = 0.05/8 = 0.00625$ for segmentation). Effect sizes were quantified via Cohen's d (small: |d| < 0.5; medium: 0.5–0.8; large: > 0.8). Intersection-over-Union (IoU) scores assessed segmentation agreement against ground truth. OncoVision demonstrated variable confidence relative to human readers across the ten features (Extended Data Fig. 8a). Mean confidence (\pm s.d.) averaged over 100 cases was 0.871 ± 0.077 for OncoVision, compared to 0.767 ± 0.071 for juniors, 0.880 ± 0.061 for seniors, and 0.948 ± 0.046 for experts. Pairwise comparisons revealed significantly higher confidence for OncoVision versus juniors in 8/10 features (P < 0.001, Cohen's d = 0.856-2.289), mixed results versus seniors (5/10 features significant; P < 0.01, d = -1.083 to 1.033), and lower confidence versus experts in 9/10 features (P < 0.05, d = -2.076 to 0.175). Onco Vision attains higher confidence than junior radiologists and comparable levels to senior radiologists, particularly for challenging subclasses such as spiculated masses, isodense lesions, heterogeneously dense tissue, and BI-RADS 4-5 categories. Experts maintain the highest baseline confidence, with only marginal improvement from AI assistance. AI assistance markedly enhanced reader confidence (Extended Data Fig. 8b). Juniors showed the largest gains (from $0.75-0.79 \pm 0.07$ to $0.88-0.91 \pm 0.02$; P < 0.001, d > 1.3), followed by seniors $(0.88 \pm 0.06 \text{ to } 0.92 - 0.93 \pm 0.02; P < 0.001, d \approx 0.7)$. Experts exhibited no significant change $(0.93-0.96\pm0.04 \text{ to } 0.94-0.96\pm0.04; P>0.05, d<0.02)$, consistent with their high baseline performance. Diagnostic time was substantially reduced with AI assistance (Extended Data Fig. 8c). Juniors decreased from $38.8-41.5 \pm 3.6-4.0$ min to $17.0-18.6 \pm 1.4-1.7$ min per case (55-57For segmentation, OncoVision achieved superior IoU in mass regions (0.925 vs. 0.904–0.907 for radiologists; P < 0.001, d = 0.618-0.683, medium effect) but slightly lower in calcifications (0.720) vs. 0.739-0.740; P < 0.001, d = -0.362 to -0.377, small), axilla findings (0.813 vs. 0.823-0.825; P < 0.001, d = -0.232 to -0.284, small), and breast tissue (0.659 vs. 0.684; P < 0.001, d = -0.459to -0.476, small) (Extended Data Fig. 8d). AI was less distributed indicating more uniform AI. AI

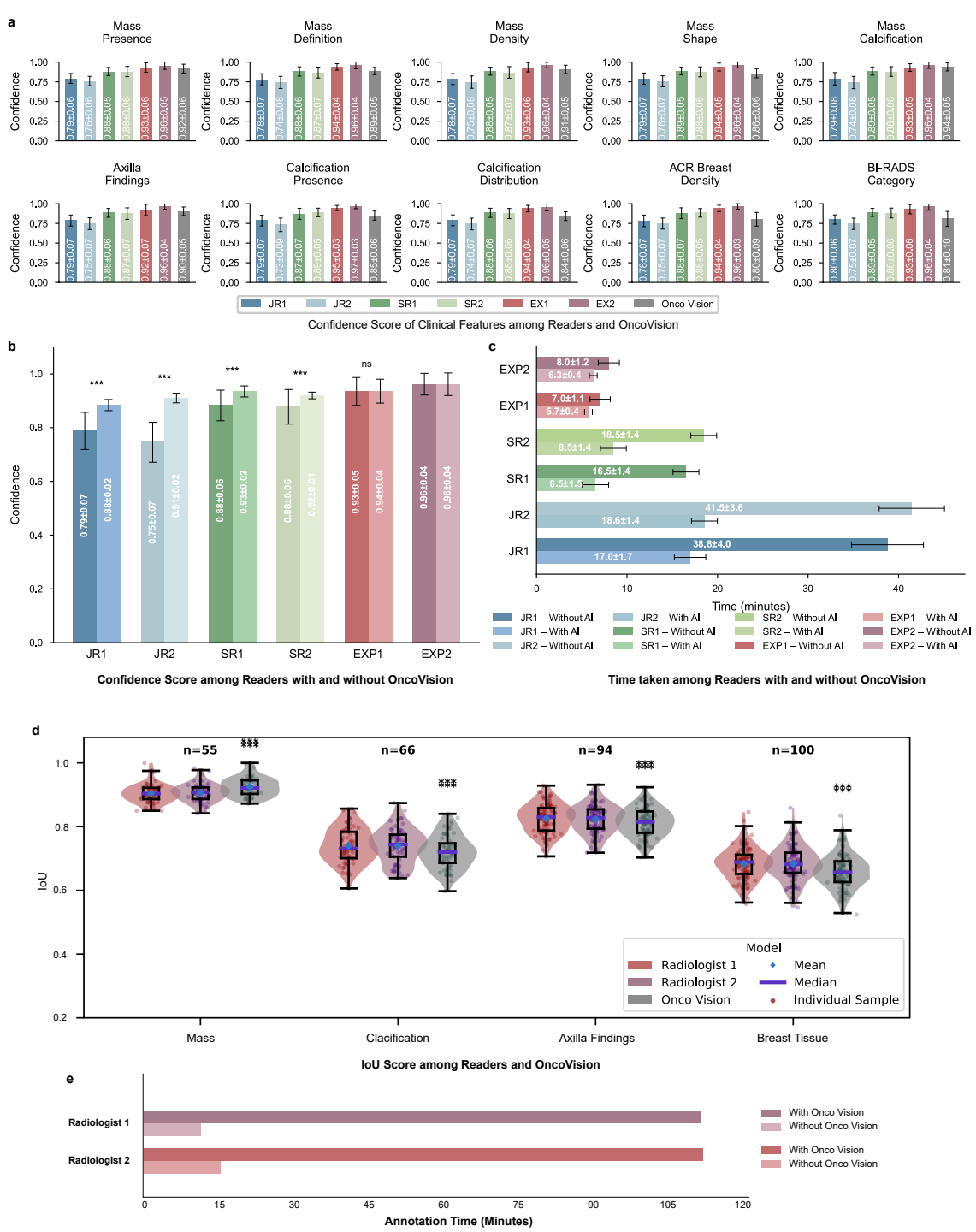


Fig. 8: Preliminary Reader Study Evaluating Diagnostic Confidence, Efficiency, and Segmentation Performance with and without OncoVision AI Assistance. (a) Mean diagnostic confidence (± 1 s.d.) across ten clinical features for six radiologists (JR1–JR2: junior; SR1–SR2: senior; EXP1–EXP2: expert) and OncoVision (n=100 cases). Asterisks denote Wilcoxon signed-rank test vs. group average (*P < 0.05, **P < 0.01, ***P < 0.001). OncoVision exceeds juniors in 8/10 features, shows mixed performance vs. seniors, and is lower than experts in 9/10. (b) Paired mean confidence (± 1 s.d.) per reader with/without AI (n=10 tasks). Onetailed Wilcoxon: juniors (**P < 0.001, Cohen's d > 1.3), seniors (P < 0.001, $d \approx 0.7$), experts (P > 0.05). (c) Mean diagnostic time (± 1 s.d.) with/without AI. OncoVision reduces time by 55–61% (juniors/seniors) and 18–22% (experts). (d) Violin–box plots of IoU across four regions (n=100). OncoVision outperforms radiologists in mass (0.925 vs. 0.904–0.907; $P < 1.56 \times 10^{-4}$, Bonferroni-corrected Wilcoxon), though lower in tissue and calcification regions. (e) Mean segmentation time per batch: ~ 120 min without AI vs. ~ 10 –15 min with AI.

reduced segmentation time to 10–15 min with AI (Extended Data Fig. 8e), underscoring efficiency gains. OncoVision proves, in this reader study, to be a robust decision-support tool by increasing confidence, decreasing time and providing best discrete lesion segmentation for junior and senior radiologists. For specialists, it provides incremental usefulness and hybrid human-AI strategies may be recommended for best clinical integration. These results validate OncoVision 's promise to minimize inter-observer variability and improve fair and equal access to high quality breast cancer diagnostics.

Feature	Late Fusion Variant	Class	†Precision	\uparrow Recall	$\begin{array}{c} \uparrow F1 \\ \mathbf{Score} \end{array}$	↑Accuracy	
	Independent	No	0.9379	0.9555	0.9466	0.9390	
Mass	Independent	Yes	0.9404	0.9174	0.9174 0.9288		
Presence	Dependent	No	0.9397	0.9485	0.9441	0.9363	
	Dependent	Yes	0.9319	0.9205	0.9262	0.9505	
	Independent	Absent	0.9362	0.9625	0.9492		
	Independent	Well-defined	0.8286	0.9022	0.8638	0.8952	
	Independent	Ill-defined	0.8615	0.6154	0.7179	0.0302	
Mass	Independent	Spiculated	1.0000	0.4545	0.6250		
Definition	Dependent	Absent	0.9338	0.9578	0.9457		
	Dependent	Well-defined	0.7752	0.8889	0.8282	0.8740	
	Dependent	Ill-defined	0.8727	0.5275	0.6575	0.8740	
	Dependent	Spiculated	0.6667	0.1818	0.2857		
	Independent	Absent	0.9300	0.9649	0.9471		
	Independent	Low-dense	0.8964	0.9301	0.9129	0.0151	
	Independent	Isodense	0.8642	0.8537	0.8589	0.9151	
Mass	Independent	High-dense	0.9459	0.5932	0.7292		
Density	Dependent	Absent	0.9318	0.9602	0.9458		
	Dependent	Low-dense	0.8872	0.9301	0.9081	0.9019	
	Dependent	Isodense	0.8310	0.7195	0.7712		
	Dependent	High-dense	0.7917	0.6441	0.7103		
	Independent	Absent	0.9302	0.9672	0.9483		
	Independent	Oval	0.8417	0.8298	0.8357	0.0000	
	Independent	Round	0.6364	0.3590	0.4590	0.8806	
Mass	Independent	Irregular	0.8054	0.8163	0.8108		
Shape	Dependent	Absent	0.9342	0.9649	0.9493		
	Dependent	Oval	0.7708	0.7872	0.7789	0.0094	
	Dependent	Round	0.7143	0.2564	0.3774	0.8634	
	Dependent	Irregular	0.7613	0.8027	0.7815		
	Independent	No	0.9633	0.9955	0.9791	0.0000	
Mass	Independent	Yes	0.9583	0.7340	0.8313	0.9629	
${\bf Calcification}$	Dependent	No	0.9719	0.9970	0.9843		
	Dependent	Yes	0.9740	0.7979	0.8772	0.9721	
	Independent	No	0.9288	0.9235	0.9261		
Axillary	Independent	Yes	0.9330	0.9377	0.9353	0.9310	
Findings	Dependent	No	0.8877	0.9405	0.9133		
	Dependent	-		0.9403 0.8953	0.9193	0.9164	
	-	No					
Calcification	Independent	Yes	$0.8653 \\ 0.8889$	0.9299 0.7949	0.8964 0.8393	0.8740	
Calcification Presence		109	0.0009	0.1343	0.0030		
Presence	Dependent	No	0.8628	0.8824	0.8725		

Continued on next page

Table 2 – continued from previous page

Feature	Late Fusion Variant	Class	†Precision	↑Recall	↑F1 Score	†Accuracy
	Dependent	Yes	0.8278	0.8013	0.8143	
	Independent	Absent	0.8568	0.9365	0.8949	
	Independent	Discrete	0.8514	0.7560	0.8008	0.8594
	Independent	Cluster/Grouped	0.9268	0.7170	0.8085	0.0001
	Independent	Line/Segmental	0.8889	0.8000	0.8421	
Distribution	Dependent	Dependent Absent		0.8844	0.8696	
	Dependent	Discrete	0.7680	0.7680	0.7680	0.8329
	Dependent	Cluster/Grouped	0.9524	0.7547	0.8421	0.0023
	Dependent	Line/Segmental	1.0000	0.6000	0.7500	
	Independent	Fatty/Normal	0.8400	0.7400	0.7900	
	Independent	Fibroglandular/ Mixed	0.7900	0.8000	0.7900	0.7745
	Independent	Heterogeneously Dense	0.7900	0.8800	0.8400	
	Independent	Highly Dense	0.6800	0.5400	0.6000	
Density	Dependent	Fatty/Normal	0.8313	0.8178	0.8245	
	Dependent	Fibroglandular/ Mixed	0.6951	0.7653	0.7285	0.7653
	Dependent	Heterogeneously Dense	0.7742	0.7500	0.7619	
	Dependent	Highly Dense	0.9500	0.5000	0.6552	
	Independent	1	0.6905	0.8529	0.7632	
	Independent	2	0.7628	0.7126	0.7368	
	Independent	3	0.8013	0.6983	0.7463	0.7660
	Independent	4	0.7899	0.7833	0.7866	0.7000
	Independent	5	1.0000	0.5556	0.7143	
BI-RADS	Independent	6	1.0000	0.5938	0.7451	
Category	Dependent	1	0.6784	0.8067	0.7370	
	Dependent	2	0.6975	0.6766	0.6869	
	Dependent	3	0.7935	0.6872	0.7365	0.7281
	Dependent	4	0.7692	0.7500	0.7595	0.,201
	Dependent	5	0.8333	0.5556	0.6667	
	Dependent	6	0.8400	0.6563	0.7368	

Continued on next page

Table 2 – continued from previous page

Feature	$egin{array}{c} ext{Late Fusion} \ ext{Variant} \end{array}$	\uparrow Precision \uparrow Recall $\frac{\uparrow F1}{\text{Score}} \uparrow$ Accuracy
---------	--	---

Table 2: This table provides a detailed analysis of the classification performance results for two late fusion variants: Independent and Dependent, when predicting breast cancer diagnosis associated clinical features. The analysis involves 10 clinical features that include Mass Presence, Mass Definition, Mass Density, Mass Shape, Mass Calcification, Axillary Findings for calcifications presence-calcification distribution-ACR breast density-B-IRADS Category. For each feature the precision, recall, and F1 score for their respective classes are compared, as well as the accuracy (where applicable) with upward arrows (\(\gamma\)) representing desirably larger values for model performance. The Independent variant consistently outperforms the Dependent one across many features, especially in difficult multi-class cases. For example, for Mass Presence prediction, the Dependent variant achieves F1 score of 0.926 (as opposed to 0.929 for dependent variant), while returning marginally lower recall for "Yes" class (0.920 against 0.917). Mass Calcification: Independent variant also performs better than the Dependent counterpart for Mass Calcification, with an F1 score of 0.877 (\uparrow) compared to 0.831, mainly due to higher precision (0.974 vs. 0.958) and recall (0.798 vs. 734). Dependent also in particular excels at detecting calcifications, a key diagnostic factor, this is particularly high for Mass Calcification with accuracies of 0.972 (†). In multi-class problems, as in Mass Definition and Mass Shape model performances varies across variants. Mass Definition Independent vs Dependent: The overall accuracy of the independent is 0.874 (\downarrow) compared to the dependent's 0.895, as a result of lower recall for class "Spiculated" (0.182 vs 0.455). But it demonstrates a higher precision for the 'Well-defined' category (0.775 vs. 0.829). Also in the case of Mass Shape independent variant attains an F1 score equal to 0.781 (\downarrow) for the "Irregular" class against 0.811 of our dependent variant, meaning trade-offs regarding difficult morphological patterns are being made. Regarding Axillary Findings, the Dependent variant has less accurate (0.916 vs 0.931), but more precise (0.945 vs 0.933) "Yes" class prediction, indicating a conservative prediction strategy relative to Independent manner that would not allow inappropriate treatment assignments for an ambiguous case with respect to negative findings in axillae in early stage breast cancer assessment by imaging. Regarding Calcification Distribution, the Independent variant performs equally compared to its Dependent counterpart with an F1 score of 0.842 (\gamma) for the "Cluster/Grouped" class versus 0.809 in its discriminated alternative. ACR Breast Density and BI-RADS Category predictions reflect substantial difficulty, especially for classes "Highly Dense" and "BI-RADS 5". The Independent variant obtains a significantly F1 score of 0.655 (†) in "Highly Dense" than the Accordant variant, while using larger recall (0.500 vs. 0.540). For BI-RADS Category, however, both architectures fail to achieve high F1 scores (with once again poor results for imbalanced classes such as "BI-RADS 5" and "BI-RADS 6" reaching a peak of approximately 0.75, indicating that further optimization is still required when dealing with imbalances in the dataset.

References

- [1] Ferlay, J., Colombet, M., Soerjomataram, I., Parkin, D.M., Piñeros, M., Znaor, A., Bray, F.: Global cancer statistics 2020: Globocan estimates of incidence and mortality worldwide for 36 cancers in 185 countries. CA: A Cancer Journal for Clinicians 71(3), 209–249 (2021) https://doi.org/10.3322/caac.21660
- [2] Wilkinson, L., Gathani, T.: Understanding breast cancer as a global health concern. British Journal of Radiology 95(1130), 20211033 (2022) https://doi.org/10.1259/bjr.20211033 https://academic.oup.com/bjr/article-pdf/95/1130/20211033/57372848/bjr.20211033.pdf
- [3] Siegel, R.L., Miller, K.D., Wagle, N.S., Jemal, A.: Cancer statistics, 2023. CA: A Cancer Journal for Clinicians 73(1), 17–48 (2023) https://doi.org/10.3322/caac.21763
- [4] World Health Organization: Global Breast Cancer Initiative: Breast Cancer Fact Sheet 2020 (2020). https://www.who.int/news-room/fact-sheets/detail/breast-cancer

- [5] D'Orsi, C.J., Sickles, E.A., Mendelson, E.B., Morris, E.A.: ACR BI-RADS Atlas: Breast Imaging Reporting and Data System, 5th edn. American College of Radiology, Reston, VA (2013). Accessed: 2025-09-22. https://www.acr.org/Clinical-Resources/Reporting-and-Data-Systems/Bi-Rads
- [6] Sickles, E.A., D'Orsi, C.J.: Acr bi-rads mammography. ACR BI-RADS Atlas: Breast Imaging Reporting and Data System, 1–134 (2013). Accessed: 2025-09-22
- [7] Liberman, L., Menell, J.H.: Breast imaging reporting and data system (bi-rads). Radiologic Clinics of North America 40(3), 409-430 (2002) https://doi.org/10.1016/S0033-8389(01) 00017-3
- [8] Elmore, J.G., Wells, C.K., Lee, C.I., Howard, D.H., Feinstein, A.R.: Variability in radiologists' interpretations of mammograms. New England Journal of Medicine 331(22), 1493–1499 (2009) https://doi.org/10.1056/NEJM199412013312206
- [9] Lehman, C.D., Arao, R.F., Sprague, B.L., Lee, J.M., Buist, D.S.M., Kerlikowske, K., Henderson, L.M., Onega, T., Tosteson, A.N.A., Rauscher, G.H., Miglioretti, D.L.: National performance benchmarks for modern screening mammography. Radiology 283(1), 49–58 (2016) https://doi.org/10.1148/radiol.2016161174
- [10] Barlow, W.E., White, E., Ballard-Barbash, R., Vacek, P.M., Titus-Ernstoff, L., Carney, P.A., Tice, J.A., Buist, D.S., Geller, B.M., Rosenberg, R., et al.: Prospective breast cancer risk prediction model for women undergoing screening mammography. Journal of the National Cancer Institute 98(17), 1204–1214 (2006) https://doi.org/10.1093/jnci/djj331
- [11] Birdwell, R.L., Ikeda, D.M., O'Shaughnessy, K.F., Sickles, E.A.: Mammographic characteristics of 115 missed cancers later detected with screening mammography and the potential utility of computer-aided detection. Radiology **219**(1), 192–202 (2001) https://doi.org/10.1148/radiology.219.1.r01ap16192
- [12] Pace, L.E., Keating, N.L.: A systematic assessment of benefits and risks to guide breast cancer screening decisions. JAMA **311**(13), 1327–1335 (2014) https://doi.org/10.1001/jama. 2014.1398 https://jamanetwork.com/journals/jama/articlepdf/1853165/jrv140002.pdf
- [13] Perry, N., Broeders, M., Wolf, C., Törnberg, S., Holland, R., Karsa, L.: European guidelines for quality assurance in breast cancer screening and diagnosis. Annals of Oncology 19(4), 614–622 (2008) https://doi.org/10.1093/annonc/mdm481
- [14] Ciecierski-Holmes, T., Singh, R., Axt, M., Brenner, S., Barteit, S.: Artificial intelligence for strengthening healthcare systems in low-and middle-income countries: a systematic scoping review. NPJ digital medicine 5(1), 162 (2022)
- [15] Bamodu, O.A., Chung, C.-C.: Cancer care disparities: overcoming barriers to cancer control in low-and middle-income countries. JCO Global Oncology 10, 2300439 (2024)
- [16] Hosny, A., Parmar, C., Quackenbush, J., Schwartz, L.H., Aerts, H.J.W.L.: Artificial intelligence in radiology. Nature Reviews Cancer 18(8), 500–510 (2018) https://doi.org/10.1038/s41568-018-0016-5
- [17] Topol, E.J.: High-performance medicine: The convergence of human and artificial intelligence. Nature Medicine **25**(1), 44–56 (2019) https://doi.org/10.1038/s41591-018-0300-7
- [18] Shen, L., Margolies, L.R., Rothstein, J.H., Fluder, E., McBride, R., Sieh, W.: Deep learning to improve breast cancer detection on screening mammography. Scientific reports **9**(1), 12495 (2019)
- [19] Kelly, C.J., Karthikesalingam, A., Suleyman, M., Corrado, G., King, D.: Key challenges for delivering clinical impact with artificial intelligence. BMC Medicine 17, 195 (2019) https:

//doi.org/10.1186/s12916-019-1426-2

- [20] Kaushal, A., Altman, R., Langlotz, C.: Geographic distribution of us cohorts used to train deep learning algorithms. Jama **324**(12), 1212–1213 (2020)
- [21] Reyes, M., Meier, R., Pereira, S., Silva, C.A., Dahlweid, F.-M., Tengg-Kobligk, H., Summers, R.M.: On the interpretability of artificial intelligence in radiology: Challenges and opportunities. Radiology: Artificial Intelligence 2(3), 190043 (2020) https://doi.org/10.1148/ryai. 2020190043
- [22] Tonekaboni, S., Joshi, S., McCradden, M.D., Goldenberg, A.: What clinicians want: Contextualizing explainable machine learning for clinical end use. Proceedings of Machine Learning Research 106, 359–380 (2019)
- [23] Vellido, A.: The importance of interpretability and visualization in machine learning for applications in medicine and health care. Neural computing and applications **32**(24), 18069–18083 (2020)
- [24] Rajpurkar, P., Irvin, J., Ball, R.L., Zhu, K., Yang, B., Mehta, H., Duan, T., Ding, D., Bagul, A., Langlotz, C.P., Patel, B.N., Yeom, K.W., Shpanskaya, K., Blankenberg, F.G., Seekins, J., Amrhein, T.J., Mong, D.A., Halabi, S.S., Zucker, E.J., Ng, A.Y., Lungren, M.P.: Chexnet: Radiologist-level pneumonia detection on chest x-rays with deep learning. arXiv (2017) https://doi.org/10.48550/arXiv.1711.05225
- [25] Arun, N., Gaw, N., Singh, P., Chang, K., Aggarwal, M., Chen, B., Hoebel, K., Gupta, S., Patel, K., Gidwani, M., Adebayo, J., Li, M.D., Kalpathy-Cramer, J.: Assessing the trustworthiness of saliency maps for localizing abnormalities in medical imaging. Radiology: Artificial Intelligence 3(6), 200267 (2021) https://doi.org/10.1148/ryai.2021200267
- [26] Wubineh, B.Z., Deriba, F.G., Woldeyohannis, M.M.: Exploring the opportunities and challenges of implementing artificial intelligence in healthcare: A systematic literature review. In: Urologic Oncology: Seminars and Original Investigations, vol. 42, pp. 48–56 (2024). Elsevier
- [27] Whitworth, P., Vicini, F., Valente, S.A., Brownson, K., DuPree, B., Kohli, M., Lawson, L., Shah, C.: Reducing rates of chronic breast cancer–related lymphedema with screening and early intervention: an update of recent data. Journal of Cancer Survivorship 18(2), 344–351 (2024)
- [28] Gastounioti, A., Desai, S., Ahluwalia, V.S., Conant, E.F., Kontos, D.: Artificial intelligence in mammographic phenotyping of breast cancer risk: a narrative review. Breast Cancer Research **24**(1), 14 (2022)
- [29] Yang, F., Xiong, D., Liao, L., Lu, X., Zhang, H., Li, X., Huang, L.: The comparative clinical value of mammography, ultrasound, and magnetic resonance imaging in predicting the efficacy of neoadjuvant chemotherapy for breast cancer in radiological diagnosis. International Journal of Clinical and Experimental Medicine Research 9(3) (2025)
- [30] Schaffter, T., Buist, D.S.M., Lee, C.I., Nikulin, Y., Ribli, D., Salcudean, S.E., Kim, E., Gimenez, F., Lotter, W., Berkowitz, S.J., et al.: Evaluation of combined artificial intelligence and radiologist assessment to interpret screening mammograms. JAMA Network Open 3(3), 200265 (2020) https://doi.org/10.1001/jamanetworkopen.2020.0265
- [31] Tao, X., Gandomkar, Z., Li, T., Brennan, P.C., Reed, W.M.: Radiomic analysis of cohort-specific diagnostic errors in reading dense mammograms using artificial intelligence. British Journal of Radiology **98**(1165), 75–88 (2025)
- [32] Barrio, A.V., Van Zee, K.J.: Controversies in the treatment of ductal carcinoma in situ. Annual review of medicine **68**(1), 197–211 (2017)

- [33] Leeuwen, M.M., Doyle, S., Belt–Dusebout, A.W., Mierden, S., Loo, C.E., Mann, R.M., Teuwen, J., Wesseling, J.: Clinicopathological and prognostic value of calcification morphology descriptors in ductal carcinoma in situ of the breast: a systematic review and meta-analysis. Insights into Imaging 14(1), 213 (2023)
- [34] Brackstone, M., Baldassarre, F.G., Perera, F., Cil, T., Dayes, I., Engel, J., Kornecki, A., George, R., SenGupta, S.K., Eisen, A.: Management of the axilla in early-stage breast cancer. Journal of Clinical Oncology 39(27), 3056–3082 (2021) https://doi.org/10.1200/JCO.21.00934
- [35] Beatty, J., Morrow, M., Ballman, K.V., Shak, S., Theriault, R.L.: Axillary nodal evaluation in breast cancer: State of the art. Radiology **296**(3), 515–528 (2020) https://doi.org/10.1148/radiol.2020192534
- [36] Kim, S., Tran, T.X.M., Kim, M.K., Chung, M.S., Lee, E.H., Lee, W., Park, B.: Associations between breast cancer risk factors and mammographic breast density in a large cross-section of korean women. European Journal of Cancer Prevention 33(5), 407–413 (2024)
- [37] Boyd, N.F., Guo, H., Martin, L.J., Sun, L., Stone, J., Fishell, E., Jong, R.A., Hislop, G., Chiarelli, A., Minkin, S., et al.: Mammographic density and the risk and detection of breast cancer. New England journal of medicine **356**(3), 227–236 (2007)
- [38] Zhou, Z., Siddiquee, M.M.R., Tajbakhsh, N., Liang, J.: Unet++: A nested u-net architecture for medical image segmentation. Deep Learning in Medical Image Analysis and Multimodal Learning for Clinical Decision Support 11045, 3–11 (2018) https://doi.org/10.1007/978-3-030-00889-5_1
- [39] Baccouche, A., Garcia-Zapirain, B., Castillo Olea, C., Elmaghraby, A.S.: Connected-unets: a deep learning architecture for breast mass segmentation. NPJ Breast Cancer 7(1), 151 (2021)
- [40] Samala, R.K., Chan, H.P., Hadjiiski, L.M.: Deep learning in mammography: diagnostic accuracy of a multipurpose image analysis system. Academic Radiology **25**(7), 893–905 (2018)
- [41] Song, Q., diFlorio-Alexander, R.M., Sieberg, R.T., Dwan, D., Boyce, W., Stumetz, K., Patel, S.D., Karagas, M.R., MacKenzie, T.A., Hassanpour, S.: Automated classification of fat-infiltrated axillary lymph nodes on screening mammograms. The British Journal of Radiology 96(1151), 20220835 (2023)
- [42] Gudhe, N.R., Behravan, H., Sudah, M., Okuma, H., Vanninen, R., Kosma, V.-M., Mannermaa, A.: Area-based breast percentage density estimation in mammograms using weight-adaptive multitask learning. Sci. Rep. 12, 12060 (2022) https://doi.org/10.1038/s41598-022-16141-2
- [43] Singh, V.K., Rashwan, H.A., Romani, S., Akram, F., Pandey, N., Sarker, M.M.K., Saleh, A., Arenas, M., Arquez, M., Puig, D., et al.: Breast tumor segmentation and shape classification in mammograms using generative adversarial and convolutional neural network. Expert Systems with Applications 139, 112855 (2020)
- [44] Tong, Y., Jiang, J., Chen, F., Guo, G., Zhang, C., Deng, T.: A novel approach for segmentation and quantitative analysis of breast calcification in mammograms. Frontiers in Oncology 14, 1281885 (2024)
- [45] Tan, H., Wu, Q., Wu, Y., Zheng, B., Wang, B., Chen, Y., Du, L., Zhou, J., Fu, F., Guo, H., et al.: Mammography-based artificial intelligence for breast cancer detection, diagnosis, and birads categorization using multi-view and multi-level convolutional neural networks. Insights into Imaging 16(1), 109 (2025)
- [46] Leeds, I., Sharma, P., Garg, M.: Interobserver variability in microcalcification interpretation: implications for ai development. Breast Journal **26**(8), 1543–1549 (2020)

- [47] Ronneberger, O., Fischer, P., Brox, T.: U-net: Convolutional networks for biomedical image segmentation. In: International Conference on Medical Image Computing and Computer-assisted Intervention, pp. 234–241 (2015). Springer
- [48] Ahmed, I., Hossain, M.T., Nahid, M.Z.I., Sanjid, K.S., Junayed, M.S.S., Uddin, M.M., Khan, M.M.: Pioneering precision in lumbar spine mri segmentation with advanced deep learning and data enhancement. Machine Learning with Applications 20, 100635 (2025) https://doi.org/10.1016/j.mlwa.2025.100635

5 Extended Data

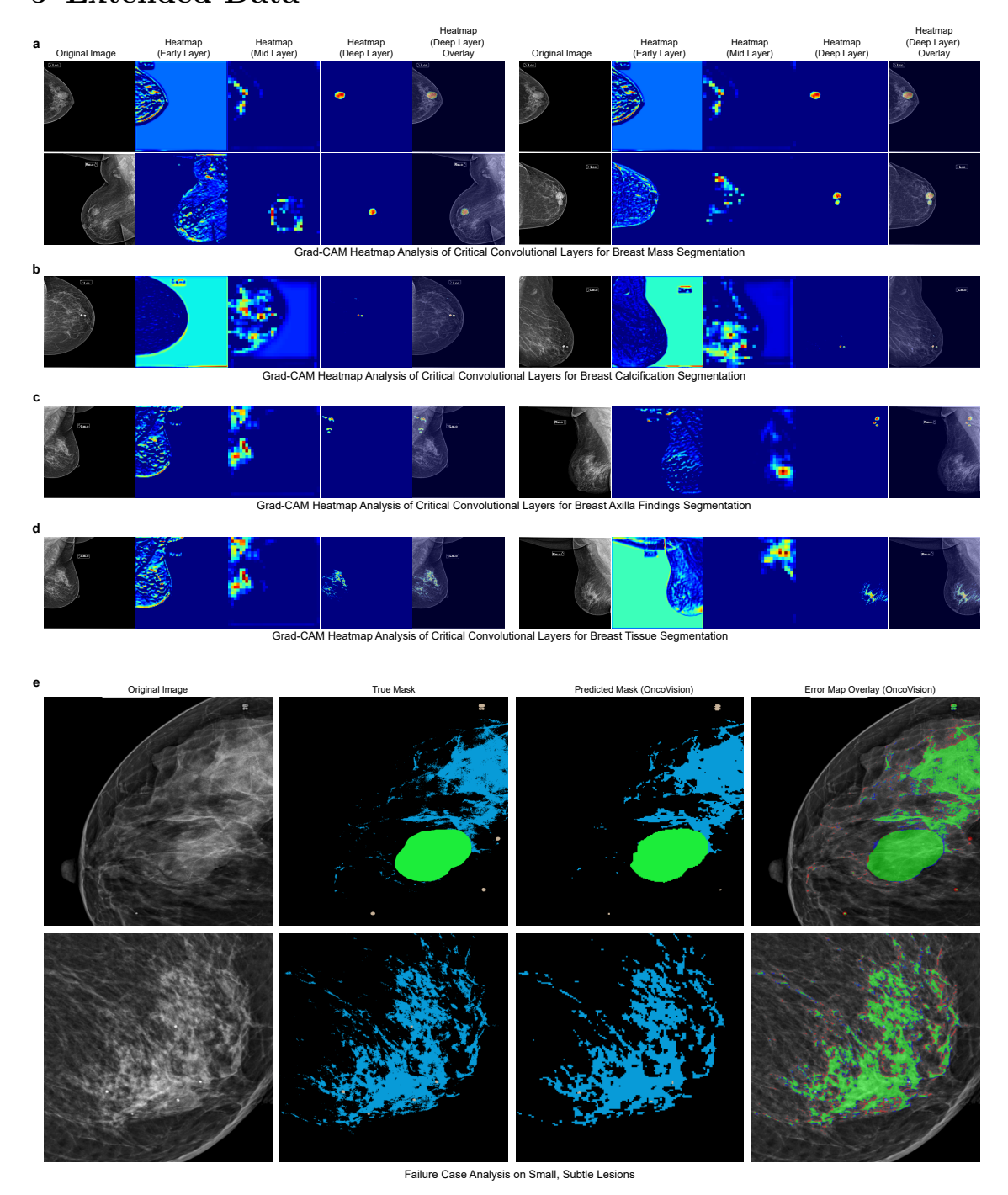


Fig. 9: Grad-CAM analysis and failure case evaluation for OncoVision

(a-d) Gradient-weighted Class Activation Mapping (Grad-CAM) visualizations across multiple convolutional layers conv2D_5 (early), conv2D_11 (mid), and conv2D_19 (deep) overlaid on original mammograms to illustrate spatial attention patterns during segmentation of mass (a), calcification (b), axilla findings (c), and breast tissue (d). Warm colors indicate regions with high gradient contribution to the prediction, revealing progressive refinement of attention from coarse localization in early layers to fine boundary delineation in deeper layers. The model consistently highlights anatomically relevant regions, with strong activation at lesion margins and internal structures, demonstrating alignment between learned features and clinical morphology.

e. Error map analysis of two failure cases involving low-contrast microcalcifications composed of only a few pixels (1–3 px in diameter), overlaid on original mammograms. High-resolution insets (zoomed 8–10×) reveal that predicted masks miss subtle clusters with minimal intensity deviation from background tissue ($\Delta I < 5$ HU equivalent). These lesions occupy < 0.1% of the total image area and exhibit near-noise-level pixel values, making them difficult to distinguish even for expert radiologists. The errors highlight the fundamental challenge of segmenting sub-visual, low-contrast calcifications at the limits of mammographic resolution, a known source of false negatives in both human and AI-based detection.

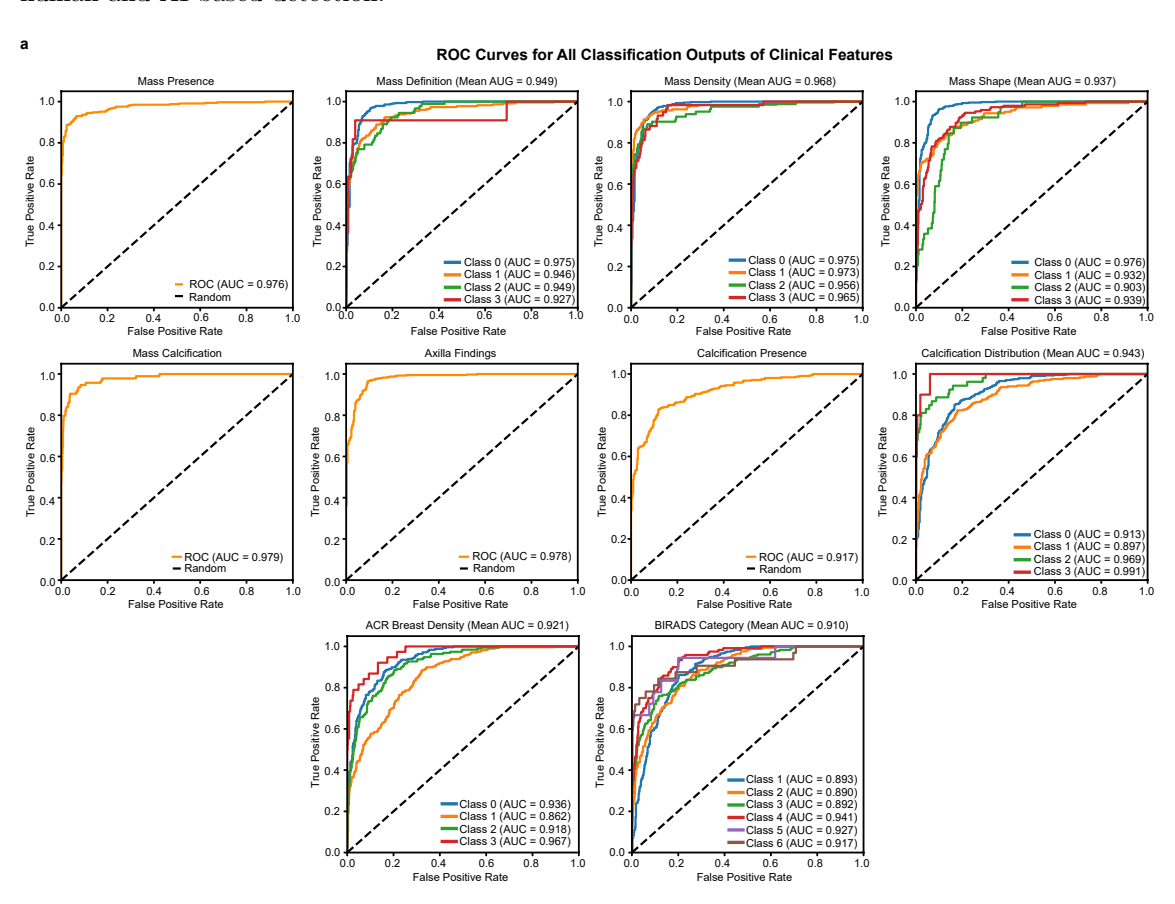


Fig. 10: Diagnostic performance across clinical features for the late fusion independent variant.

a. Receiver operating characteristic (ROC) curves for ten clinical diagnostic tasks in breast mammography, including morphological, density, and categorical assessments. Each curve represents the one-versus-rest classification performance for a specific class within a task. Area under the ROC curve (AUC) values are reported with 95% confidence intervals estimated via 1000 bootstrap samples. The model achieves high discriminative accuracy across all tasks, with AUCs exceeding 0.90 for mass presence, mass definition, mass density, mass shape, mass calcification, axilla findings, and calcification distribution. Performance is robust across subtypes, including spiculated (0.927), irregular (0.939), and segmental (0.991) calcifications, as well as BI-RADS category 4 (0.941) and

5 (0.927). Confidence intervals reflect the large test cohort (n = 754 per task), demonstrating statistical reliability. The high AUCs and narrow confidence bounds validate the model's ability to support fine-grained diagnostic reasoning in a multimodal reporting pipeline.

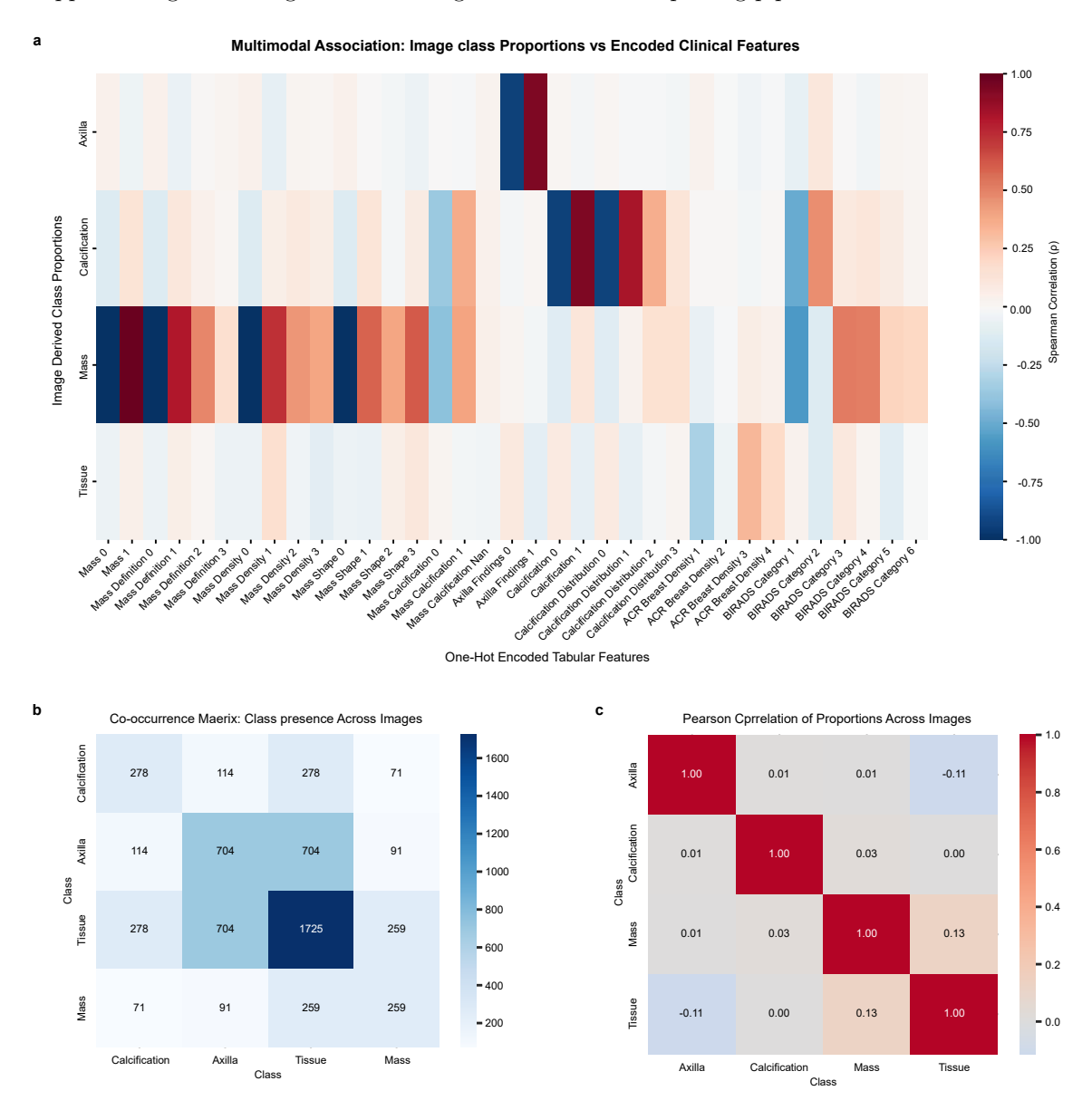


Fig. 11: Multimodal associations and inter-class relationships across the segmentation and clinical feature datasets.

a. Heatmap of multimodal associations showing the relationship between image-derived class proportions and encoded clinical/tabular features. The y-axis represents per-image segmentation class proportions for Axilla findings, Calcification, Mass, and Tissue derived from mask annotations, while the x-axis shows one-hot encoded clinical features including Mass Presence, Mass Definition, Mass Density, Mass Shape, Mass Calcification, Axilla Findings, Calcification Presence, Calcification Distribution, ACR Breast Density, and BI-RADS category. Spearman correlation coefficients are calculated for each class-feature pair, highlighting the degree to which image-based features align with corresponding clinical annotations. This panel provides an integrated view of the multimodal dataset, revealing patterns of co-dependency between image-derived and tabular clinical features, which can guide feature selection and model interpretability. b. Class co-occurrence heatmap depicting the frequency with which multiple segmentation classes appear simultaneously within individual masks. Each cell represents the proportion of images in which a given pair of

classes co-occur, thereby highlighting patterns of overlap or mutual exclusivity between segmentation classes. This visualization helps identify potential dependencies among classes, informs data augmentation strategies, and aids in understanding the natural co-distribution of classes in the dataset. c. Pearson correlation heatmap of per-image segmentation class proportions across all masks. Each cell indicates the correlation between two classes' proportions within images, providing insight into potential redundancy or inverse relationships among segmentation classes. High positive or negative correlations may indicate systematic patterns in the dataset that need to be accounted for during modeling, whereas near-zero correlations reflect independence between class distributions. Together, panels a—c emphasize both the multimodal integration of image and tabular features and the statistical relationships between segmentation classes, illustrating the complex structure and balance of the dataset.

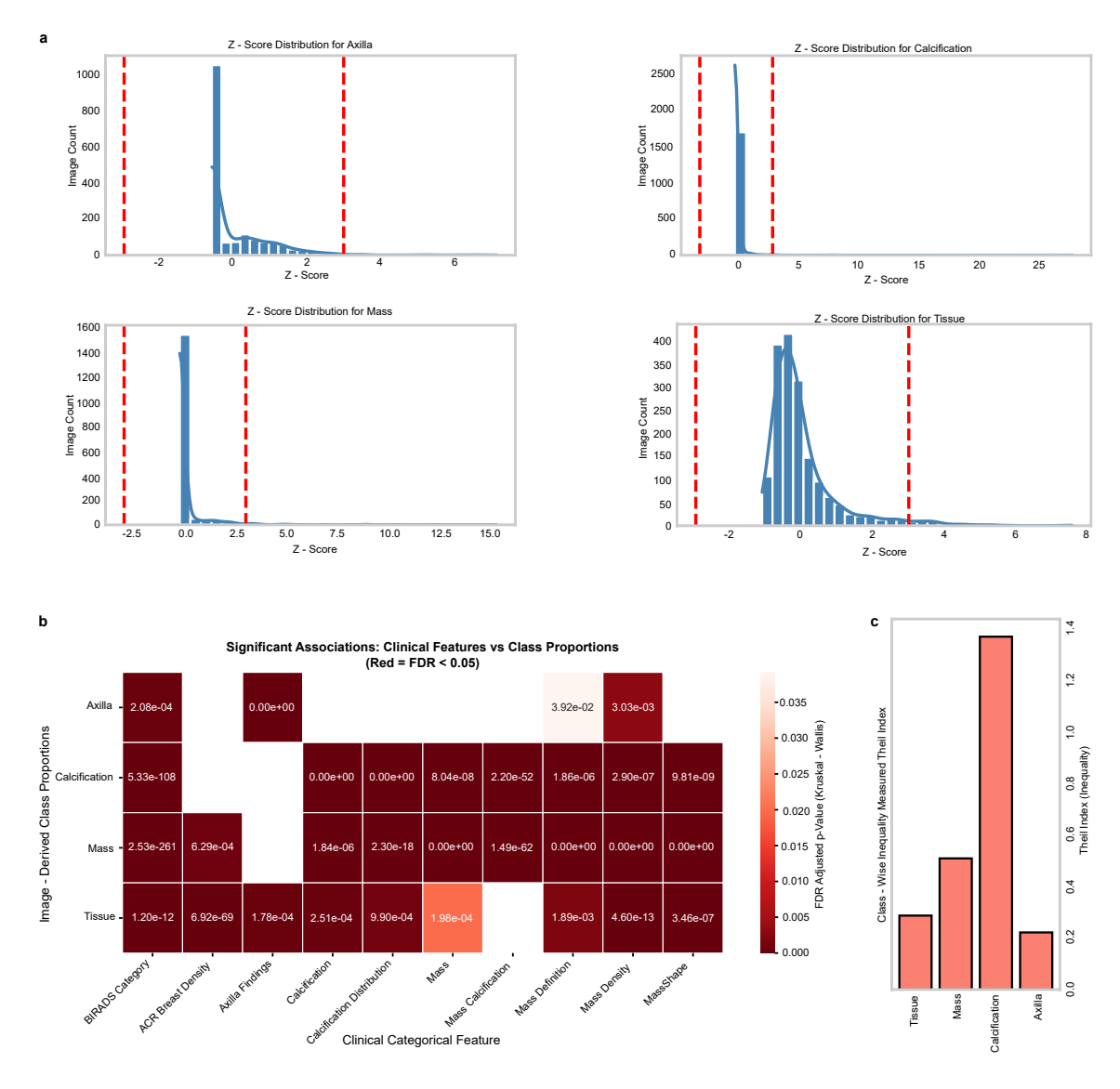


Fig. 12: Statistical integrity, distributional inequalities, and significant associations across segmentation and clinical features.

a. Z-score distribution histograms for each segmentation class (Axilla findings, Calcification, Mass, Tissue) depict the standardized per-image class proportions across the dataset. The y-axis represents the number of images, and the x-axis corresponds to the Z-scores of class proportions. These histograms identify outliers and unusual distributions, providing a quantitative check on the effects of augmentation and dataset balancing. By visualizing deviations from the mean, these plots help assess whether the class proportions remain consistent and whether the augmentation

successfully mitigates class imbalance while preserving natural variability. b. Heatmap of significant associations between clinical/tabular features and segmentation class proportions, based on Kruskal-Wallis tests with False Discovery Rate (FDR) adjustment. The y-axis represents per-image class proportions derived from segmentation masks, and the x-axis shows categorical clinical features including Mass Presence, Mass Definition, Mass Density, Mass Shape, Mass Calcification, Axilla Findings, Calcification Presence, Calcification Distribution, ACR Breast Density, and BI-RADS category. Each cell is colored according to the FDR-adjusted p-value (red = FDR ; 0.05, white = FDR ; 0.035), indicating which clinical features significantly associate with specific imagederived class proportions. This panel emphasizes the statistical rigor of the dataset, highlighting strong multimodal relationships and guiding downstream modeling choices. c. Horizontal bar plot of Theil index values quantifying class-wise inequality across the dataset. The Theil index measures unevenness in class representation, where higher values indicate greater disparity. Class-wise indices are as follows: Axilla findings = 0.222, Calcification = 1.368, Mass = 0.509, Tissue = 0.287. This visualization provides insight into inherent imbalances within the dataset, identifying classes that remain underrepresented or overrepresented, and guiding targeted augmentation or weighting strategies for model training. Together, panels a-c provide a comprehensive view of the statistical distribution, significance of feature-class associations, and inequality in class representation, supporting data quality assessment and ensuring that augmentation strategies effectively balance the dataset while maintaining biological and clinical relevance.



Fig. 13: Multimodal overview of tabular features by BI-RADS category and embedding alignment before and after augmentation.

(a-b) Grouped stacked bar plots illustrating the distribution of tabular/clinical features across BI-RADS categories, shown separately for pre (a) and post-augmentation (b) datasets. For each of the nine tabular features—including Mass Presence, Mass Definition, Mass Density, Mass Shape, Mass Calcification, Axilla Findings, Calcification Presence, Calcification Distribution, and ACR Breast Density—stacked bars represent the proportion of subcategories within each BI-RADS class. The pre-augmentation plots (left panel) reveal the original distribution of tabular features across BI-RADS categories, highlighting inherent imbalances and skewed representations. The post-augmentation plots (right panel) demonstrate how augmentation balances these distributions, ensuring that feature representation is more uniform and mitigating potential bias in downstream

model training. By providing a side-by-side comparison, these plots allow assessment of augmentation efficacy in aligning tabular features with clinically meaningful categories. **c.** Multimodal UMAP embedding of combined image-derived and tabular features, colored by BI-RADS category, comparing pre and post-augmentation datasets. The embedding visually captures the similarity and alignment of high-dimensional data across modalities, showing how augmentation affects the joint distribution of image and tabular features. Pre-augmentation embeddings reveal the natural clustering of cases based on BI-RADS categories, while post-augmentation embeddings show enhanced density and overlap across clusters, indicating improved balance and representation of underrepresented categories. This multimodal visualization provides a clinically meaningful perspective on dataset structure, demonstrating that augmentation preserves intrinsic relationships while reducing class imbalance, and facilitates downstream tasks such as classification or risk stratification. Together, panels **a** and **b** offer a comprehensive view of the impact of augmentation on tabular feature distributions and multimodal embedding space, ensuring both clinical and statistical integrity while maintaining alignment between image-derived and encoded features.

Class	Metric	Mean Difference	SD	LoA Lower	LoA Upper	95% CI Lower	95% CI Upper	N
		Segmentation	Featu	res (Bland-A	Altman Anal	ysis)		
Calcification	IoU	-0.4041	0.3571	-1.1041	0.2958	-0.4276	-0.3806	889
Axilla Findings	IoU	+0.0792	0.2929	-0.4949	0.6532	+0.0610	+0.0973	1002
Breast Tissue	IoU	-0.0863	0.2616	-0.5990	0.4263	-0.0985	-0.0742	1780
Mass	IoU	+0.1178	0.3172	-0.5040	0.7396	+0.0973	+0.1384	918
Calcification	Dice	-0.4494	0.3811	-1.1963	0.2975	-0.4745	-0.4244	889
Axilla Findings	Dice	+0.0675	0.2835	-0.4883	0.6232	+0.0499	+0.0850	1002
Breast Tissue	Dice	-0.0389	0.2477	-0.5244	0.4466	-0.0504	-0.0274	1780
Mass	Dice	+0.0860	0.3027	-0.5073	0.6794	+0.0664	+0.1056	918
		Clinical Fe	atures	(Bland-Alti	man Analysi	s)		
Mass	Presence	+0.0148	0.0883	-0.1582	0.1879	+0.0085	+0.0212	754
Mass	Calcification	+0.0133	0.0770	-0.1376	0.1642	+0.0078	+0.0188	754
Mass	Density	+0.0297	0.1231	-0.2115	0.2709	+0.0209	+0.0385	754
Mass	Definition	+0.0323	0.1285	-0.2195	0.2841	+0.0231	+0.0415	754
Mass	Shape	+0.0402	0.1454	-0.2448	0.3252	+0.0298	+0.0506	754
Axilla Findings	_	+0.0334	0.1131	-0.1884	0.2552	+0.0253	+0.0415	754
Calcification	Presence	+0.0783	0.1442	-0.2043	0.3608	+0.0680	+0.0886	754
Calcification	Distribution	+0.0816	0.1556	-0.2233	0.3865	+0.0705	+0.0927	754
BI-RADS	Category	+0.1008	0.1683	-0.2290	0.4307	+0.0888	+0.1129	754
ACR	Breast Density	+0.1035	0.1655	-0.2209	0.4278	+0.0916	+0.1153	754

Table 3: Supplementary Data Table 2: Bland-Altman analysis of segmentation and clinical feature agreement between AI models. This table presents a comprehensive Bland-Altman assessment of agreement between the proposed OncoVision Multimodal Pipeline and the baseline UNet++ for four anatomical region segmentation tasks (calcification, axilla findings, breast tissue, mass), as well as between two variants of OncoVision—late fusion independent vs. dependent—for ten clinical diagnostic features. For each comparison, the mean difference (bias), standard deviation (SD), and limits of agreement (LoA = mean $\pm 1.96 \times$ SD) are reported, along with the 95% confidence interval (CI) of the mean bias and sample size (N). In segmentation, OncoVision shows significantly improved performance over UNet++, exhibiting positive bias in mass IoU (+0.118) and Dice (+0.086), indicating superior overlap accuracy, while reducing undersegmentation of calcifications (IoU: -0.404, Dice: -0.449), suggesting better sensitivity to subtle lesions. Conversely, it slightly underestimates breast tissue extent (IoU: -0.086), reflecting tighter boundary delineation. The narrow 95% CIs confirm high precision in estimated biases across all classes. For clinical feature confidence prediction, the late fusion variants demonstrate excellent agreement, with small mean differences (all < 0.11) and tight CIs, indicating consistent reasoning across architectural designs. Notably, higher variability is observed in calcification presence/distribution and BI-RADS category (LoA up to ± 0.43), reflecting inherent uncertainty in low-contrast or subjectively interpreted features. In contrast, binary tasks like mass presence show near-perfect agreement (mean diff = 0.015, 95% CI: [0.0085, 0.0212]). These results validate both the robustness of OncoVision's multimodal fusion strategy and its consistency across design choices, supporting its reliability in real-world deployment.

Class	Metric	Sample Size (N)	p-value	Cohen's d	Effect Size Category	Stars			
Segmentation Performance									
Axilla Findings	Dice	369	< 0.001	-0.158	Negligible	***			
Axilla Findings	IoU	369	< 0.001	-0.234	Small	***			
Breast Tissue	Dice	754	< 0.001	-0.717	Medium	***			
Breast Tissue	IoU	754	< 0.001	-0.857	Large	***			
Calcification	Dice	309	< 0.001	-0.877	Large	***			
Calcification	IoU	309	< 0.001	-0.849	Large	***			
Mass	Dice	328	< 0.001	-0.272	Small	***			
Mass	IoU	328	< 0.001	-0.346	Small	***			
		Clinical Featu	re Perfo	rmance					
Mass	Presence	754	< 0.0001	-0.168	Negligible	***			
Mass	Calcification	754	< 0.0001	-0.173	Negligible	***			
Mass	Density	754	< 0.0001	-0.242	Small	***			
Mass	Definition	754	< 0.0001	-0.251	Small	***			
Mass	Shape	754	< 0.0001	-0.276	Small	***			
Axilla Findings	_	754	< 0.0001	-0.295	Small	***			
Calcification	Presence	754	< 0.0001	-0.543	Medium	***			
Calcification	Distribution	754	< 0.0001	-0.524	Medium	***			
BI-RADS	Category	754	< 0.0001	-0.599	Medium	***			
ACR	Breast Density	754	< 0.0001	-0.625	Medium	***			

Table 4: Supplementary Data Table 1: Statistical comparison of segmentation and clinical feature performance between OncoVision and baseline models. The table summarizes pairwise statistical comparisons between the OncoVision Multimodal Pipeline and the UNet++ baseline for segmentation performance (IoU and Dice per anatomical class), as well as between the late fusion independent and dependent variants for ten clinical diagnostic features. Results are based on Wilcoxon signed-rank tests (segmentation) or paired t-tests (clinical confidence scores), with Bonferroni correction applied for multiple comparisons ($\alpha = 0.05$ / total tests). Effect sizes were quantified using Cohen's d, interpreted as negligible (< 0.2), small (0.2-0.5), medium (0.5–0.8), or large (> 0.8). For segmentation, OncoVision demonstrated significantly higher accuracy than UNet++ across all regions, with large effect sizes in calcification (Dice: d = -0.877), breast tissue (IoU: d = -0.857), and mass (IoU: d = -0.346), indicating substantial improvements in boundary delineation and sensitivity to subtle structures. The most pronounced gains were observed in microcalcification detection, where even small absolute improvements translate to clinically meaningful lesion capture. In clinical feature prediction, the late fusion variants showed high agreement, yet statistically significant differences emerged in several tasks. Notably, calcification presence (d = -0.543), BI-RADS category (d = -0.599), and ACR breast density (d = -0.625) exhibited medium-to-large effect sizes, suggesting architectural choices influence high-stakes outputs despite similar overall accuracy. All comparisons achieved significance after correction (p < 0.0001, Bonferroni-adjusted), indicated by *** in the Stars column. Sample sizes reflect available test instances per class. Negative Cohen's d values indicate that OncoVision outperformed the comparator (i.e., higher IoU/Dice or confidence alignment).

6 Supplementary Information

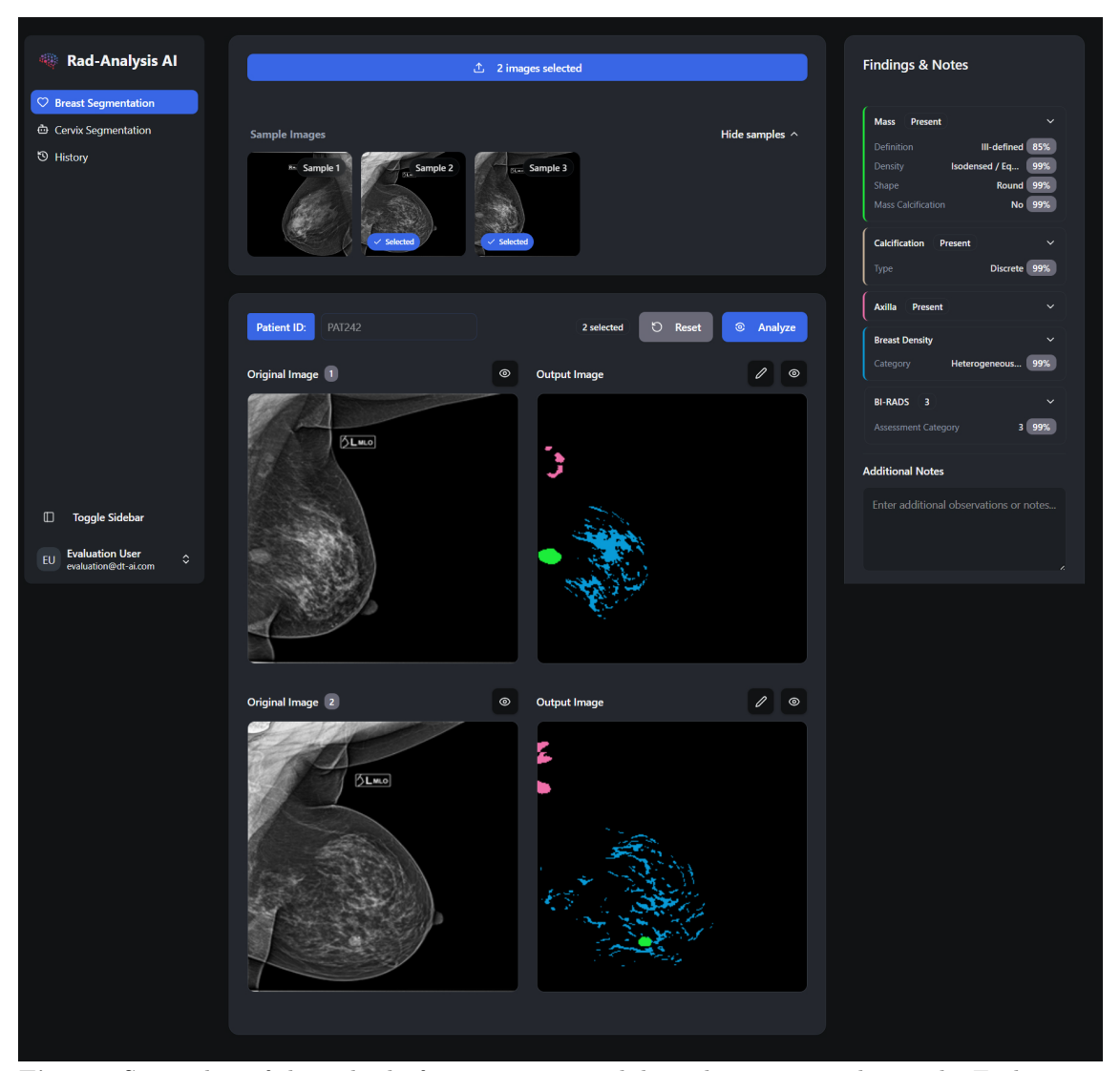


Fig. 14: Screenshot of the web platform processing a bilateral mammographic study. Each image displays high-resolution segmentation masks for mass (green), calcification (cream), axilla findings (pink), and breast tissue (blue), overlaid on the original mammogram with interactive zoom, hover and, pan via WebGL in the right sidebar, presents prediction from the late fusion independent variant of ten clinical features with confidence scores, including mass presence, definition, density, shape, calcification status and distribution, axilla findings, ACR breast density, and BI-RADS category. A downloadable PDF report compiles all outputs, including per-image visualizations, structured predictions, Gradient-weighted Class Activation Mapping (Grad-CAM) heatmaps (toggleable across early, mid, and bottleneck layers) highlight regions driving predictions, such as lesion boundaries and microcalcification clusters, and metadata, ensuring clinical traceability and integration.

Feature	Mean AUC	Class	Class Name	95% CI Lower	95% CI Upper
mass presence	0.976	N/A		0.968	0.983
	0.975	0		0.965	0.984
	0.946	1	well defined	0.928	0.962
mass definition	0.949	2	ill-defined	0.932	0.964
	0.927	3	spiculated	0.905	0.947
	0.949	Mean		0.938	0.958
	0.975	0		0.966	0.983
mass density	0.973	1	low dense	0.963	0.981
mass delicity	0.956	2	isodense/equal dense	0.942	0.969
	0.965	3	high dense	0.954	0.975
	0.967	Mean		0.959	0.974
	0.976	0		0.967	0.984
	0.932	1	oval	0.915	0.948
mass shape	0.903	2	round	0.882	0.923
	0.939	3	irregular	0.923	0.954
	0.938	Mean		0.927	0.948
mass calcification	0.979	N/A		0.972	0.985
axilla findings	0.978	N/A		0.970	0.985
calcification presence	0.917	N/A		0.898	0.934
	0.913	0		0.892	0.932
Calcification	0.897	1	discrete	0.874	0.918
Distribution	0.969	2	cluster/grouped	0.956	0.980
Distribution	0.991	3	line/segmental	0.985	0.995
	0.942	Mean		0.932	0.951
	0.936	0	fatty/normal	0.920	0.951
ACR breast density	0.862	1	fibroglandular/mixed fatty and fibroglandular	0.836	0.886
ACIT Dreast density	0.918	2	heterogeneously densed	0.900	0.935
	0.967	3	highly densed	0.957	0.976
	0.921	Mean	- •	0.911	0.930
	0.893	0	1	0.872	0.912
	0.890	1	2	0.868	0.910
	0.892	2	3	0.870	0.912
BI-RADS Category	0.941	3	4	0.926	0.955
	0.927	4	5	0.910	0.942
	0.917	5	6	0.898	0.934
	0.910	Mean		0.898	0.921

Table 5: Extended Data Table 3: Diagnostic performance of the OncoVision Multimodal Pipeline (Late Fusion Independent Variant) across ten clinical features. The table presents the area under the receiver operating characteristic curve (AUC) for each clinical feature predicted by the OncoVision Multimodal Pipeline (Late Fusion Independent Variant) on an independent test set (n = 754). For binary tasks (e.g., mass presence), AUC reflects overall discriminative ability. For multi-class attributes (e.g., mass shape, BI-RADS category), AUC is computed per class using the one-vs-rest approach and reported alongside class labels and integer codes. Mean AUC across all classes is provided as a summary metric where applicable. OncoVision achieves excellent discriminative performance across all tasks, with mean AUC ≥ 0.91 for every feature. It excels in high-sensitivity tasks such as mass calcification (AUC = 0.979) and axilla findings (AUC = 0.978), critical for early cancer detection and staging. Morphological assessments—including mass definition (mean AUC = 0.949), density (0.967), and shape (0.938)—show strong agreement with radiologist-level reasoning, particularly for spiculated (0.927) and irregular (0.939) forms associated with malignancy. Notably, the model demonstrates exceptional accuracy in complex, fine-grained classifications, such as calcification distribution (AUC = 0.991 for line/segmental patterns) and ACR breast density (AUC = 0.967 for highly dense tissue), which are particularly challenging due to low contrast. BI-RADS category predictions exceed AUC = 0.89 for all categories, with peak performance in Category 4 (0.941) and 5 (0.927), indicating robust risk stratification capability. All estimates include two-sided 95% confidence intervals based on DeLong's method, confirming statistical reliability and validating OncoVision as a comprehensive, accurate, and trustworthy AI system capable of generating structured diagnostic reports from mammographic images alone.

Statistic	Axilla Findings		Calcifi	Calcification		Mass		sue
Statistic	Before	After	Before	After	Before	After	Before	After
Mean ↑	0.0019	0.0020	0.0001	0.0002	0.0015	0.0045	0.0244	0.0260
Median ↑	0.0000	0.0000	0.0000	0.0000	0.0000	0.0000	0.0183	0.0180
Mode ↑	0.0000	0.0000	0.0000	0.0000	0.0000	0.0000	0.0079	0.0141
Variance ↑	0.0000	0.0000	0.0000	0.0000	0.0000	0.0001	0.0005	0.0006
Std. Dev. \uparrow	0.0032	0.0032	0.0005	0.0010	0.0057	0.0095	0.0215	0.0252
Min	0.0000	0.0000	0.0000	0.0000	0.0000	0.0000	0.0001	0.0001
Max ↑	0.0252	0.0261	0.0139	0.0142	0.0896	0.0942	0.1874	0.1965
Skewness \downarrow	2.5965	2.5826	23.4045	12.6271	7.3255	4.0442	2.6367	2.4242
Kurtosis ↓	10.1455	9.9347	612.9674	169.3061	73.4795	22.0749	9.2344	7.5731
Gini Index ↓	0.7384	0.7190	0.9541	0.8985	0.9297	0.7913	0.4032	0.4525
Entropy ↑	6.3352	7.8937	4.2596	6.4797	5.0483	7.6160	7.1661	8.5737

Table 6: Summary statistics of key imaging features before and after data augmentation. All values are rounded to four decimal places. This table reports descriptive statistics for four primary feature categories: Axilla Findings, Calcification, Mass, and Tissue. For each feature category, mean, median, mode, variance, standard deviation, minimum, maximum, skewness, kurtosis, Gini index, and entropy are reported. Post-augmentation, the mean and standard deviation increased slightly across all feature categories, reflecting the inclusion of previously underrepresented instances (e.g., the mean for Mass features increased from 0.0015 to 0.0045). Skewness and kurtosis for Calcification and Mass decreased (e.g., Calcification kurtosis decreased from 612.9674 to 169.3061), indicating reduced extreme outliers and a more normalized distribution. Gini indices decreased across categories (e.g., Mass from 0.9297 to 0.7913), demonstrating improved equality of feature representation, while entropy values increased (e.g., Axilla Findings from 6.3352 to 7.8937), reflecting greater diversity. The min-max ranges expanded modestly, particularly for Mass and Tissue, confirming that rare but clinically relevant instances were added. Overall, this table demonstrates that augmentation enhanced the representational balance and heterogeneity of imaging features, supporting more robust AI model training across diverse BI-RADS categories.

Category Before Augmentation After Augmentatio							
Image Class Occurrence							
Calcification	278 (16.12%)	3115 (41.34%)					
Axilla Findings	704 (40.81%)	3523 (46.76%)					
Tissue	1725 (100%)	7535 (100%)					
Mass	259 (15.01%)	3403 (45.16%)					
	Unique Class count po	er mask					
1 class	737	808					
2 classes	758	3822					
3 classes	207	2496					
4 classes	23	409					

Table 7: Image class distribution and multi-class mask complexity before and after augmentation. This table provides a comprehensive summary of how targeted augmentation affected the representation of segmentation classes and the diversity of multi-class masks in the dataset. The top section ("Image Class Occurrence") enumerates the total number of images containing each segmentation class—Calcification, Axilla, Tissue, and Mass—along with their corresponding proportions relative to the full dataset. Before augmentation, several critical classes such as Calcification and Mass were severely underrepresented, comprising only 16.1% and 15.0% of images, respectively, whereas Tissue was fully represented across all images (100%). Post-augmentation, the total image counts and proportions for all classes increased substantially, reflecting a more balanced dataset; for example, Calcification rose to 41.3% and Mass to 45.2%, while Axilla and Tissue also showed proportional increases (46.8% and 100%, respectively), ensuring the model is exposed to sufficient examples of each class during training. The bottom section ("Multi-Class Mask Complexity") details the number of images grouped by the number of unique segmentation classes present within individual masks, highlighting multi-class complexity. Prior to augmentation, images containing only a single class accounted for 737 instances, while those containing two or more classes (multi-class masks) were less frequent, with 207 images containing three classes and only 23 images containing all four classes. Following augmentation, multi-class diversity was substantially enhanced: images with two classes increased to 3,822, three-class masks to 2,496, and four-class masks to 409. This expansion not only increases the dataset size but also promotes richer spatial and morphological variation, enabling the model to better learn the interactions and co-occurrence patterns of multiple tissue types and abnormalities. Overall, this table demonstrates that augmentation not only balances individual class representation but also significantly improves the diversity and complexity of segmentation masks, which is critical for robust multi-class segmentation in mammography.

Ranl	k Dependent V	ariant Independent Variant	Before Augmen	tation	After Augmentation		
100111	a Dependent .	aram masponaem varam	Kruskal-Wallis H	Adj. p	Kruskal-Wallis H	Adj. p	
1	Mass	Mass shape	1686.56	< 0.001	6624.14	< 0.001	
2	Calcification	Calcification Presence	1491.79	< 0.001	6343.56	< 0.001	
3	Axilla	Axilla Findings	1491.21	< 0.001	5368.70	< 0.001	
4	Mass	Mass Density	1685.58	< 0.001	6615.37	< 0.001	
5	Mass	Mass Definition	1685.58	< 0.001	6611.10	< 0.001	
6	Calcification	Calcification Distribution	1492.34	< 0.001	6382.91	< 0.001	
7	Mass	Mass Presence	1685.55	< 0.001	6597.75	< 0.001	
8	Mass	BI-RADS Category	1221.99	< 0.001	5300.60	< 0.001	
9	Calcification	BI-RADS Category	513.08	< 0.001	2003.37	< 0.001	
10	Breast Tissue	ACR breast density	321.99	< 0.001	2136.22	< 0.001	

Table 8: Top 10 significant multimodal associations between image-derived segmentation proportions and key clinical features before and after augmentation. This table presents the results of Kruskal-Wallis tests identifying statistically significant associations between the proportions of segmentation classes in imaging data (dependent variables) and tabular clinical features (independent variables), with false discovery rate (FDR)-adjusted p-values. The left half ("Before Augmentation") shows baseline associations, while the right half ("After Augmentation") demonstrates how these associations were affected by targeted data augmentation. Prior to augmentation, Mass exhibited strong associations with intrinsic morphological characteristics, including mass shape, density, and definition, highlighting the importance of capturing structural heterogeneity in training data. Calcification and Axilla also demonstrated significant associations with their respective clinical features (calcification type and axilla findings), whereas Tissue showed moderate associations with breast density (rank 10). Notably, the H statistics for these associations reflect the relative effect sizes, with Mass \sim mass shape and Calcification \sim calcification Presence yielding the highest values, confirming their dominant role in multimodal relationships. Following augmentation, all key associations were preserved and substantially strengthened, as reflected by marked increases in the H statistics—for instance, the association Mass \sim mass shape increased from 1686.56 to 6624.14. Augmentation also enabled previously moderate associations to rise in prominence, such as Tissue with ACR breast density (H = $321.99 \rightarrow 2136.22$), and reinforced links between Calcification, Mass, and BI-RADS categories. These changes indicate that augmentation not only increases sample representation for underrepresented features but also enhances statistical power, resulting in more robust, reproducible, and biologically meaningful multimodal relationships. All associations remain highly significant (adjusted (Adj.) p < 0.001), demonstrating that the synthetic data supports the development of clinically interpretable AI models while maintaining fidelity to established imaging-clinical correlations.

		Before	Augmentation	After Augmentation		
Features	Sub Categories	Count	Percentage	Count	Percentage	
Mass Presence	Yes	260	15.1	3395	45.1	
wass Presence	No	1465	84.9	4140	54.9	
	Well Defined	182	10.6	2389	31.7	
Mass Definition	Ill-Defined	70	4.1	904	12.0	
	Spiculated	8	0.5	102	1.4	
	Low Dense	153	8.9	1964	26.1	
Mass Density	Isodense	60	3.5	822	10.9	
	High Dense	47	2.7	609	8.1	
	Oval	109	6.3	1444	19.2	
Mass Shape	Round	47	2.7	577	7.7	
	Irregular	104	6.0	1374	18.2	
Mass Calcification	Yes	48	2.8	878	11.7	
Wass Calcincation	No	1676	97.2	6657	88.3	
A :11 T2: 1:	Yes	724	42.0	3912	51.9	
Axilla Findings	No	1001	58.0	3623	48.1	
Clic ii D	Yes	291	16.9	3075	40.8	
Calcification Presence	No	1434	83.1	4460	59.2	
	Discrete	249	14.4	2461	32.7	
Calcification Distribution	Cluster	36	2.1	510	6.8	
	Line	7	0.4	115	1.5	
	Fatty/Normal	589	34.1	2355	31.3	
ACR Breast Density	Fibroglandular/Mixed	665	38.6	2945	39.1	
ACIT Breast Density	Heterogeneously Dense	407	23.6	1923	25.5	
	Highly Dense	64	3.7	312	4.1	
	1	1137	65.9	2255	29.9	
	2	276	16.0	1724	22.9	
BI-RADS Category	3	167	9.7	1789	23.7	
DI-ITADS Category	4	98	5.7	1236	16.4	
	5	17	1.0	233	3.1	
	6	30	1.7	298	4.0	

Table 9: Distribution of key tabular clinical features before and after data augmentation. The table summarizes counts and percentages for each subcategory across 10 clinical features, including Mass presence, definition, density, shape, and calcification, Axilla findings, Calcification presence and distribution, ACR breast density, and BI-RADS category. Augmentation substantially increases the representation of underrepresented categories (e.g., Spiculated mass: $0.5\% \rightarrow 1.4\%$, Clustered calcification: $2.1\% \rightarrow 6.8\%$) while preserving the relative distribution of common classes. This expansion ensures more balanced coverage of clinically relevant phenotypes, enhancing the robustness of multimodal AI model training.